

VISUAL QUALITY METRICS RESULTING FROM DYNAMIC CORNEAL

TEAR FILM TOPOGRAPHY

by

Cameron Cole Solem

A Thesis Submitted to the Faculty of the

COLLEGE OF OPTICAL SCIENCES

In Partial Fulfillment of the Requirements

For the Degree of

MASTER OF SCIENCE

In The Graduate College

THE UNIVERSITY OF ARIZONA

2017

STATEMENT BY AUTHOR

The thesis titled "Visual Quality Metrics Resulting from Dynamic Corneal Tear Film Topography" prepared by Cameron Solem has been submitted in partial fulfillment of requirements for a master's degree at the University of Arizona and is deposited in the University Library to be made available to borrowers under rules of the Library.

Brief quotations from this thesis are allowable without special permission, provided that an accurate acknowledgement of the source is made. Requests for permission for extended quotation from or reproduction of this manuscript in whole or in part may be granted by the head of the major department or the Dean of the Graduate College when in his or her judgment the proposed use of the material is in the interests of scholarship. In all other instances, however, permission must be obtained from the author.

SIGNED: Cameron Solem

APPROVAL BY THESIS DIRECTOR

This thesis has been approved on the date shown below:

John E. Greivenkamp
Professor of Optical Sciences

Date

ACKNOWLEDGEMENTS

I would like to thank the following people for their support during the completion of this project:

To my girlfriend Kayla, my brother Aaron, and my parents Anthony and Cynthia whose love formed a foundation for me to attempt this journey.

I would like to express my deep gratitude to my advisor Dr. John Greivenkamp, for trusting me with this great opportunity, and whose patience, understanding and insight I could not have completed this thesis without.

I am also thankful to the funding sponsor of this project, Johnson & Johnson Vision Care, for which this research would not be possible.

I'm indebted to my teachers and classmates, especially Dr. Schwiegerling, Jason Micali, Chris Guido, Janelle Pilar, and David Sommitz. Their scientific intuition and passion for learning made it easy to keep going.

To my friends and former colleagues at L-3 Aeromet who gave me my first chance and taught me how to be a scientist.

To my future employer Apple for giving me a good reason to finish.

And a great thanks to all other friends and classmates for their emotional support.

Contents

1.0 METHOD.....	8
1.1 INTRODUCTION.....	8
1.1.1 GOAL	8
1.1.2 THE INTERFEROMETRIC CORNEAL TOPOGRAPHER	9
1.1.3 FOURIER ANALYSIS METHOD	12
1.2 DIFFRACTION THEORY.....	13
1.3 DFT AND ZERO PADDING	15
1.4 IMAGING THEORY	16
2.0 VERIFICATION.....	19
2.1 DIFFRACTION LIMITED AIRY DISK.....	19
2.2 SEIDEL ABERRATIONS.....	22
2.3 EYE MODELS.....	23
2.3.1 ARIZONA EYE MODEL.....	23
2.3.2 TYPICAL HUMAN EYE ABERRATION MODEL	24
2.4 THE TEAR FILM	29
2.4.1 WAVEFRONT SCALING	29
2.4.2 THE INCOHERENT PSF	33
2.4.3 THE MODULATION TRANSFER FUNCTION	34
3.0 ANALYSIS SOFTWARE	38
3.1 MOVIE SOFTWARE	39
3.2 POST PROCESSING SOFTWARE	41
3.2.1 SQF FILTER.....	43
3.2.2 STANDARD DEVIATION FILTER.....	48
3.2.3 COMBO FILTER	55
3.2.4 OTHER OPTIONS.....	56
3.2.5 END CONDITIONS.....	56
4.0 RESULTS.....	59
4.1 MOVIES AND SQF CHARTS	59
4.1.1 SUBJECT 002.....	60
4.1.2 SUBJECT 007.....	64

4.1.3 SUBJECT 009.....	66
4.1.4 SUBJECT 010.....	69
5.0 POTENTIAL IMPROVEMENTS	72
6.0 CONCLUSIONS.....	74
7.0 REFERENCES	77

List of Figures

Figure 1.1) Instantaneous Corneal Topographer	9
Figure 1.2) ICT layout (top). surface (red), cat's eye (green), fixation (yellow)	10
Figure 2.1) Incoherent Point Spread Function for a diffraction limited system (Left); also known as the Airy disk. Line Profile of the same function (Right)	20
Figure 2.2) MTF for a diffraction limited system	21
Figure 2.3) 1λ of W020 results in a well-known PSF pattern, shown in both TFI analysis software (Left) and Voelz's code (Right).....	22
Figure 2.4) AZEM wavefront OPD in pupil (4.5 mm Pupil Diameter).....	24
Figure 2.5) Typical Human Eye Aberration Model wavefront OPD in pupil (4.5 mm Pupil Diameter).....	26
Figure 2.6) The TH model wavefront (Left), the Zernike fit (Right), and the difference between the two (Bottom) (5.7 mm Pupil Diameter)	28
Figure 2.7) Tear Film data produced by the TFI (Left) (6.0 mm Pupil Diameter), windowed down (Right) (4.5 mm Pupil Diameter).....	29
Figure 2.8) Arizona Eye Model wavefront OPD for two different corneal topographies, without (Left) and with the tear film (Right) (4.5 mm Pupil Diameter)	30
Figure 2.9) Tear film wavefront OPD from residual AZEM (Left) and from TFI (Right) (4.5 mm Pupil Diameter)	31
Figure 2.10) Differences in the two Figure 2.9 wavefront OPDs (Left) and a residual fit (Right) (4.5 mm Pupil Diameter)	32
Figure 2.11) AZEM tear film wavefront OPD (Left), the TFI tear film wavefront OPD (Right), and the difference (Bottom) (4.5 mm Pupil Diameter).....	33
Figure 2.12) The incoherent produced by the TFI Software (Left) and the one produced by ZEMAX FFT software (Right).	34
Figure 2.13) The MTF is related to the Fourier transform of the incoherent PSF	35
Figure 3.1) Analysis GUI for TFI data.....	39
Figure 3.2) Single frame snapshot of the visual quality movie	41
Figure 3.3) Load post processing variables GUI	42
Figure 3.4) Post-processing GUI.....	42
Figure 3.5) SQF (average) chart [frames 150 and 153 highlighted]	43
Figure 3.6) Movie Snapshots for frames 150 (top) and 153 (bottom) shown in Figure 3.5	44
Figure 3.7) SQF charts, with (bottom) and without (top) SQF filtering	46
Figure 3.8) Standard Deviation for each frame over entire collect - unfiltered	49
Figure 3.9) Movie snapshot for frame 774 highlighted in Figure 3.8	50

Figure 3.10) Standard Deviation for each frame over entire collect – 1 st pass StDev	51
Figure 3.11) Movie snapshot for frame 513 highlighted in Figure 3.11	52
Figure 3.12) Standard Deviation for each frame over entire collect – 2 nd pass StDev.....	53
Figure 3.13) Standard Deviation for each frame over entire collect – auto standard deviation filter	54
Figure 3.14) SQF charts: Unfiltered (top), SQF filtered (left), standard deviation filtered (right), and combo filter (bottom)	55
Figure 3.15) Post processing end condition GUI.....	57
Figure 3.16) Post Processing script cycle	57
Figure 3.17) Subject 002 – 201508 – Collect 4: This step in the analysis helps the user determine if the filter conditions set previously were acceptable.	58
Figure 4.1) Subject 002 – 201508 – Collect 4 SQF Chart Total collection time: 27 seconds.....	61
Figure 4.2) Subject 002 – 201508 – Collect 8 SQF Chart Total collection time: 31 seconds.....	63
Figure 4.3) Subject 007 – Collect 1 SQF Chart Total collection time: 120 seconds.....	65
Figure 4.4) Subject 009 – 201507 – Collect 3 SQF Chart Total collection time: 91 seconds.....	67
Figure 4.5) Subject 009 – 201507 – Collect 8 SQF Chart Total collection time: 40 seconds.....	68
Figure 4.6) Subject 010 – 20150513 – Collect 12 SQF Chart Total collection time: 64 seconds.....	70
Figure 4.7) Movie Snapshots for frames 1041 (top) and 1152 (bottom) for Subject 010 – Collect 12 - shown in Figure 4.6.....	71
Figure 5.1) Dry Eye Disease Cycle	73
Figure 6.1) Intensity of fluorescence or tear film thickness over time.....	75
Figure 6.2) Intensity of fluorescence or tear film thickness over time. B: lid closure; C: lid opening; B-C interval: blink.	76

List of Videos

Video 4.1) Subject 002 – 201508 – Collect 4 Movie	61
Video 4.2) Subject 002 – 201508 – Collect 8 Movie	63
Video 4.3) Subject 007 – Collect 1 Movie	65
Video 4.4) Subject 009 – 201507 – Collect 3 Movie	67
Video 4.5) Subject 009 – 201507 – Collect 8 Movie	68
Video 4.6) Subject 010 – 20150513 – Collect 12 Movie	70

List of Tables

Table 2-1) Arizona Eye Model specifications used in the following verification	20
Table 2-2) Results of analysis on a diffraction limited system with ICT analysis software.....	21
Table 2-3) Z40 coefficient results for different eye models	28
Table 2-4) Function handedness properties	37

The University of Arizona

ABSTRACT

College of Optical Sciences

Master of Science

By Cameron Solem

The visual quality effects from the dynamic behavior of the tear film have been determined through measurements acquired with a high resolution Twyman-Green interferometer. The base shape of the eye has been removed to isolate the aberrations induced by the tear film. The measured tear film was then combined with a typical human eye model to simulate visual performance. Fourier theory has been implemented to calculate the incoherent point spread function, the modulation transfer function, and the subjective quality factor for this system. Analysis software has been developed for ease of automation for large data sets, and outputs movies have been made that display these visual quality metrics alongside the tear film. Post processing software was written to identify and eliminate bad frames. As a whole, this software creates the potential for increased intuition about the connection between blinks, tear film dynamics and visual quality.

1.0 METHOD

1.1 INTRODUCTION

The human cornea is covered by several layers of different liquid materials. The summation of these layers is referred to as the tear film. The tear film introduces the highest index of refraction differential between adjacent spaces in the human eye, and so it can be said that the tear film induces the highest refractory power out of any surface in the eye. About 70% of the human eye's refractive power is due to the tear film surface (Primeau, 2011). This implies that the topography of the tear film is of great importance with regards to visual quality. The visual quality effects of the tear film have been observed but not properly characterized.

1.1.1 GOAL

The motivation for this project was to take existing tear film data and apply a set of metrics to describe the effects that dynamic tear film topography has on visual quality. Movies were to be made that showed the tear film changing alongside these visual quality metrics. It was thought that these movies would lead to greater intuition about the relationship between blinks, tear film, visual quality.

The point spread function (PSF), modulation transfer function (MTF), and subjective quality factor (SQF) were chosen. The definitions for these metrics is described in detail in Section 1.4. The PSF of an optical system allows a performance simulation of any scene using a simple convolution operation. This characteristic shows that a PSF precisely characterizes the performance of a system.

It was for this powerful reason that the PSF was chosen as the visual quality metric. The MTF and SQF are directly related to the PSF of a system. The SQF in particular provides a useful single number metric for analysis. It has been shown before that the tear film does have a significant impact on the PSF (Kasprzak & Licznarski, 1999). However this research only analyzed the visual effects of two modeled tear film surfaces. Analyzing the PSF effects of measured tear film data across many frames and many subjects could lead to stronger conclusions.

1.1.2 THE INTERFEROMETRIC CORNEAL TOPOGRAPHER

The Interferometric Corneal Topographer (ICT) is an instantaneous phase-shifting dual interferometer built to measure the corneal topography of the human eye. A more detailed explanation for this tool can be found in the references (Micali, J. D., 2015). An intuitive layout can be seen in Figure 1.1, and a much more detailed schematic can be seen in Figure 1.2.

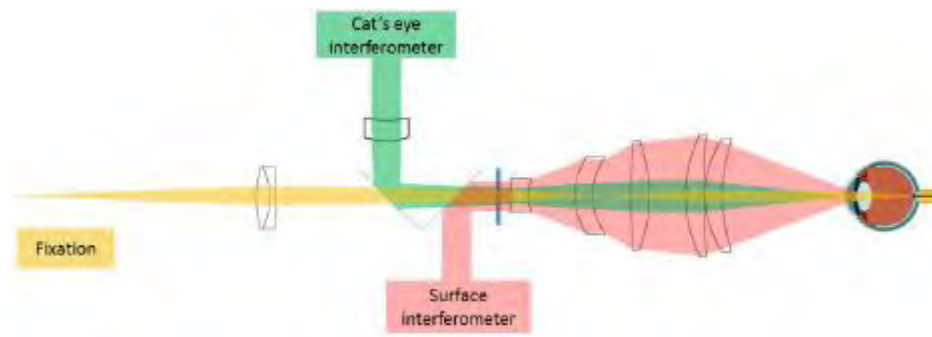


Figure 1.1) *Instantaneous Corneal Topographer*
(Micali, J. D., 2015)

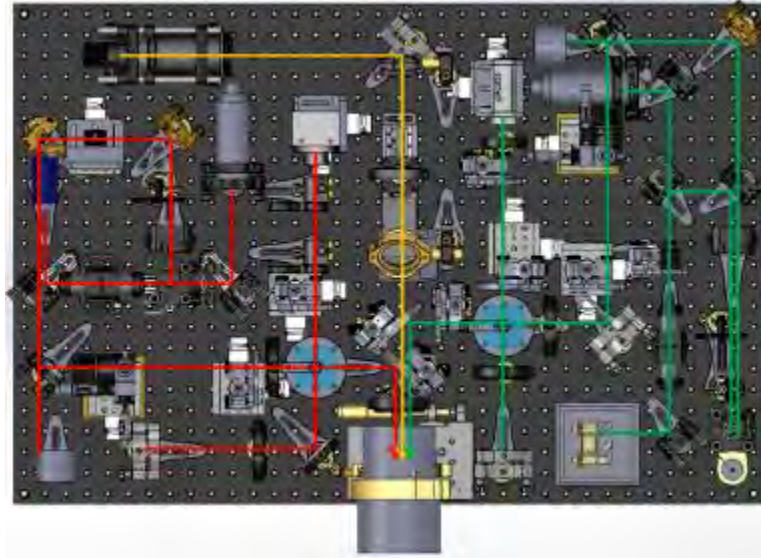


Figure 1.2) ICT layout (top). surface (red), cat's eye (green), fixation (yellow)
(Micali, J. D., 2015)

The ICT performs non null interferometry using a dual interferometer setup. The surface interferometer (Figure 1.2 – red) focuses at the center of curvature of the eye. This system will capture the topography of the eye. The cat's-eye interferometer (Figure 1.2 – green) focuses at the vertex of the eye. This systems keeps track of the position of the eye during the collect, which is useful for two reasons. The absolute position of the eye can be used to recover the base radius of curvature of the surface (Micali, J. D., 2015). The cat's eye interferometer is also necessary for the reverse ray tracing algorithm used in the ICT software. Reverse ray tracing is used to correct for retrace error induced by a non-null system. Reverse ray tracing is dependent on absolute optical path lengths, and so the absolute position of the eye must be known (Micali, J. D., 2015). The cat's eye interferometer makes this possible.

The major advantage the ICT has over commercial topographers is higher spatial and height resolution. Improved spatial resolution allows for more accurate characterization of tear film breakup features.

Almost all commercial topographers forgo the use of interferometry and instead use Placido disc setups to measure corneal topography. In addition to the complexity, cost and alignment sensitivity associated with interferometry, an additional drawback of the interferometer method is the need for phase shifting to calculate the phase profile. Phase shifting usually uses a piezo-electric transducer (PZT) to induce the needed phase changes to complete the measurement. A PZT is a mirror that uses an electrical charge to translate very small, finite steps. These small steps induce a phase change in the fringe pattern necessary for the OPD calculation algorithm. This means temporal resolution is lost between the time it takes to make PZT translations.

Since the tear film is dynamic, loss of temporal resolution is undesirable. The ICT mitigates this problem by implementing instantaneous phase shifting. The ICT uses a 4D instantaneous phase shifting pixelated camera (4D Technology Corporation, Tucson, AZ), which takes advantage of the polarization characteristics of the interferometer to induce phase changes at the detector. This means that the phase changes are made instantaneously, and no temporal resolution is lost. The temporal resolution of the ICT is now limited by the frame rate of the collection system. So that ICT has improved spatial resolution while maintaining temporal resolution. It also has the sub-micron height resolution associated with interferometry.

The ICT outputs a height map describing the corneal topography of the subject for each frame of the collect. This height map is a 1201x1201 array over a 6 millimeter measurement area, resulting in a 5-micron resolution across the eye. The data is collected at a rate of 30 frames per second (FPS).

The ICT software is capable of removing a biconic fit from the height map measurement it produces. Studies have shown that human cornea shapes vary significantly, with a reported range of radii from

6.98 to 8.73 mm (Daily & Coe, 1962; P M Kiely, Smith, & Carney, 1982). Since the scope of this project is to characterize the tear film and its effects on visual quality, the variation in eye shape from person to person has been removed from the study. Each measurement used in this study will have a 16 Zernike fit removed from the height map, so that only the remaining mid and high spatial variations of the tear film are analyzed.

Since the base cornea shape has been removed, the ICT measurements function only as a Tear Film Interferometer (TFI). For this reason, the measurement device will be referred to as the TFI for the remainder of this thesis. The TFI was the name of a previous version of the ICT, whose development was the subject of a dissertation (Primeau, 2011). The most relevant distinction between the TFI and ICT is the lack of a cat's eye interferometer in the TFI.

1.1.3 FOURIER ANALYSIS METHOD

The Fourier analysis method relies on the discrete Fourier transform (DFT) operation provided by the analysis software MATLAB. The continuous Fourier transform (Equation 1.1) and the DFT (Equation 1.2) are shown below.

$$F(\xi) = \int_{-\infty}^{\infty} f(x) e^{-j2\pi\xi x} dx \quad (1.1)$$

$$F_s(m) = \sum_{n=0}^{N-1} f(n) e^{-j2\pi\frac{mn}{N}} \quad (1.2)$$

The Fourier transform is a very powerful tool in imaging theory. In any imaging system, the focal plane and the exit pupil are Fourier transform conjugates. This rule is derived from a special case in diffraction theory called the Fresnel approximation. To arrive at the Fresnel approximation, the following conceptual foundation is provided.

1.2 DIFFRACTION THEORY

Maxwell's equations describe the behavior of electromagnetic fields. The Helmholtz equation is a differential equation derived from Maxwell's equations.

$$\nabla^2 E - \frac{n^2}{c^2} \frac{\delta^2 E}{\delta t^2} = 0 \quad (1.3)$$

Solutions to the differential Helmholtz equation describe the propagation of a wave through space. One of these solutions is called the pinhole wave, or a Huygens' wavelet, which is the derivative of a spherical wave. Any field can be described as a summation of these Huygens' wavelets. This summation can be written as a superposition integral. This integral is the basis for the Rayleigh-Sommerfeld diffraction integral (Equation 1.4).

$$U_o(\vec{r}_o) = \int_{ap} \left(-\frac{j}{\lambda} + \frac{1}{2\pi r_{os}} \right) \gamma_z \frac{e^{jk r_{os}}}{r_{os}} U_s(\vec{r}_s) d\vec{r}_s \quad (1.4)$$

The Rayleigh-Sommerfeld diffraction integral describes the propagation of a field through space. The Fresnel approximation simplifies the Rayleigh-Sommerfeld diffraction integral by making a far field approximation (though not as far as Fraunhofer). The observation plane for this project will occur at the back focal plane. This is a sufficient distance away from the aperture such that the Fresnel approximation is valid. A few key approximations reduce the integral (Equation 1.4) into Equation 1.5, where the spherical Huygens's wavelets have turned into parabolic ones. This diffraction integral can be rewritten as a Fourier transform multiplied by a Fresnel phase term (Equation 1.6).

$$U_o(\vec{r}_o) = -j \frac{e^{jkz_o}}{\lambda z_o} \int_{ap} U_s(\vec{r}_s) e^{\frac{jk}{2z_o}[(x_o-x_s)^2+(y-y_s)^2]} d\vec{x}_s d\vec{y}_s \quad (1.5)$$

$$U_o(x_o, y_o) = -j \frac{e^{jkz_o}}{\lambda z_o} e^{\frac{jk}{2z_o}(x_o^2+y_o^2)} \mathbf{F}_\eta \mathbf{F}_\xi [U_s^+(x_s, y_s) e^{\frac{jk}{2z_o}(x_s^2+y_s^2)}] \quad (1.6)$$

$\mathbf{F}_\eta \mathbf{F}_\xi$ describes the 2D Fourier transform, shown in Equation 1.7.

$$\mathbf{F}_\eta \mathbf{F}_\xi [f(x, y)] = \iint_{-\infty}^{\infty} f(x, y) e^{-j2\pi\xi x} e^{-j2\pi\eta y} dx dy \quad (1.7)$$

A lens will introduce a parabolic phase term (Equation 1.8) to the incident wave. When this field is observed at the back focal distance of the lens, the parabolic phase term cancels out with the Fresnel phase term.

$$t_{lens}(x_o, y_o) = e^{\frac{jk}{2z_o}(x_o^2+y_o^2)} \quad (1.8)$$

$$U_s^+(x_s, y_s) = U_s^-(x_s, y_s)t_{lens}(x_o, y_o) \quad (1.9)$$

$$U_o(x_o, y_o) = -j \frac{e^{jkz_o}}{\lambda z_o} e^{\frac{jk}{2z_o}(x_o^2 + y_o^2)} \mathbf{F}_\eta \mathbf{F}_\xi [U_s^+(x_s, y_s)] \quad (1.10)$$

This leaves a propagation integral that functions as a pure Fourier transform integral (Equation 1.10). The canceling effect concludes that the back focal distance of an imaging system is essentially in the Fraunhofer region. An important subtlety being that the Fourier transform here does not cause the field to switch between the spatial and the frequency domain, but simply between two spatial domains, one scaled by inverse lambda multiplied by propagation distance. This scaling satisfies the Fourier transform requirement that the two spaces have an inverse unit relationship.

1.3 DFT AND ZERO PADDING

The DFT is a modified version of a Fourier transform. The Fourier transform operates on continuous surfaces that can be broken up into infinitesimally small cuts, as can any integral.

However a computer does not have infinite RAM, and thus cannot be broken up into an infinite amount of infinitesimally small cuts. Thus any function is discretized when collected, and the continuous Fourier transform needs to be modified to account for this. The DFT is the answer to this problem. One drawback to the DFT is that any function it produces is limited by the number of points contained in the discretized input. The inverse scaling rule of Fourier transforms means that if a wide function is provided, a narrow transform will result. The 6mm magnitude of the pupil size in the eye results in an airy disk width of only 3.5 microns; a wide input resulting in a narrow output.

This means that the 5-micron resolution of the input field will not be sufficient to describe the sub-micron features of the output field. A useful technique called zero padding can be used in conjunction with the DFT to work around this issue. A 1D vector can be zero padded by adding $N/2$ zeros on each side of the vector to add a total of N points to the input, thus increasing the resolution of the output. If the resolution of the original output was d_{xi} , d_{xi} can be defined as the length of the 1D Fourier space divided by the original number of points M . When N points are added through zero padding, d_{xi} is now defined as the same unchanged length of the 1D Fourier space, but now divided by $M+N$. This makes d_{xi} smaller, increasing the resolution. This concept can be applied to a 2D space as well, as it was in this analysis. Zero padding was used to increase the spatial resolution of the results.

1.4 IMAGING THEORY

Imaging theory and the DFT provide a method to turn the field in the exit pupil into a field at the focal plane by way of the Fourier transform. The tear film surface height map occurs on top the surface of the cornea and produces a wavefront variation in the entrance pupil of the eye. To propagate the field to the exit pupil, the Rayleigh Sommerfeld diffraction equation could be used. A reference sphere would then be removed to determine the wavefront error, and the Fourier Theory outlined earlier would be used to determine the incoherent PSF. However a few simple approximations allow for far less calculation.

After a biconic fit or a 16 Zernike fit has been removed from the corneal surface, the remaining wavefront error is due to tear film variation. This wavefront error is small enough and the

propagation distance is short enough that the propagation effects from the entrance pupil to the exit pupil can be ignored. This assumption is shown to be correct in Section 2.0 of this report. The cornea is very close to the entrance pupil, so the field can be approximated as being located at the entrance pupil. These assumptions result in a simple magnification operation being the only step required in moving the tear film effects to the exit pupil, as the entrance pupil and exit pupil have different sizes.

The surface now occurs in the exit pupil of the system and the Fourier transform operation can be performed to produce the output field in the focal plane. In Equation 1.11 below, $P(x,y)$ is the pupil function and $\phi(x,y)$ is the wavefront OPD function expressed as phase.

$$PSF_{coherent}(x_2, y_2) \propto \int_{-\lambda d_1}^{+\lambda d_1} \int_{-\lambda d_1}^{+\lambda d_1} P(x, y) e^{i\phi(x, y)} dx dy \quad (1.11)$$

The field is not the function that is observable in a real system, so a conversion to irradiance must be made. This output field is referred to as the coherent Point Spread Function (PSF). Coherent systems are linear with field. The output irradiance is the coherent PSF multiplied by the conjugate of the coherent PSF, as shown in Equation 1.12 below.

$$PSF_{incoherent} = PSF_{coherent} PSF_{coherent}^* \quad (1.12)$$

This is called the incoherent PSF. Incoherent systems are linear with irradiance.

$$OTF \propto \frac{\mathbf{F}_\eta \mathbf{F}_\xi [PSF_{incoherent}]}{|\mathbf{F}_\eta \mathbf{F}_\xi [PSF_{incoherent}]|_{\xi=0, \eta=0}} \quad (1.7)$$

$$MTF = |OTF| \quad (1.14)$$

SQF is the logarithmic integration of the MTF between two spatial frequency limits (Barten 1990; Granger & Cupery, 1972). This project will use a linear integration, shown in equation 1.15.

$$SQF = \int_{\xi_1}^{\xi_2} MTF d\xi \quad (1.15)$$

The Optical Transfer Function (OTF) is the normalized Fourier transform of the incoherent PSF (Equation 1.13), and the Modular Transfer Function (MTF) is calculated by taking the magnitude of the OTF (Equation 1.14). The Subjective Quality Factor (SQF) is the area under the MTF curve (Equation 1.15). The SQF is often evaluated as the area under the MTF curve between two spatial frequency limits. The spatial frequency range chosen for this analysis was 3 to 18 cyc/degree. These values are typical for visual analysis and were suggested by our research sponsor (Barten 1990; Granger & Cupery, 1972).

The incoherent PSF is the irradiance output for a point source input in an imaging system. The Fourier theory described earlier results in many useful conclusions. Any output for an imaging system is the convolution of the input and the incoherent PSF (Equation 1.16). Using convolution theorem, it is simple to express this concept in the Fourier domain (Equation 1.17). Once a PSF for a system is determined, any output can be calculated using this theory.

$$f(x) \otimes PSF = g(x) \quad (1.16)$$

$$F(\xi) OTF = G(\xi) \quad (1.17)$$

These powerful conclusions show why the PSF, MTF, and SQF are important visual quality metrics, and why they were chosen as a focus for this project. These metrics will be used to quantify the visual degradation of the tear film over time.

2.0 VERIFICATION

2.1 DIFFRACTION LIMITED AIRY DISK

The first step in this analysis process was writing software that could analyze any wavefront sag function and produce the correct PSF and MTF output. The first function to be tested was the simplest, a planar wave, simulating zero wavefront sag in the pupil, or a smooth tear film. The Fourier transform of a circular pupil is a scaled Bessel function called the sombrero function. The sombrero function is named for the dips that occur on either side of the central peak. These dips form what is called the Airy disk. A metric for the Airy disk is the diameter of the ring that is formed by the first zero that occurs outside the central peak. The core diameter of the Airy disk value is described by the following equation:

$$D_{AiryDisk} = 2.44 * \lambda * F/\# \quad (2.1)$$

4.5 mm is a typical pupil size and will be the pupil size focused on for this report. The vitreous refractive index, exit pupil diameter, and propagation distance were all taken from the Arizona Eye

Model (J.T. Schwiegerling, 2004). The wavelength of light was chosen to be in the visible spectrum as that would best represent visual quality degradation. The specifications for this analysis are listed in the table below:

Table 2-1) Arizona Eye Model specifications used in the following verification

EP Diameter (mm)	4.5
XP Diameter (mm)	4.2
z_{xp} in air (mm)	15.28
lambda (μm)	0.55
n (vitreous)	1.336

z_{xp} is the distance between the exit pupil and the rear focal point.

Simulating a planar wave input, the following plots are produced using the analysis software:

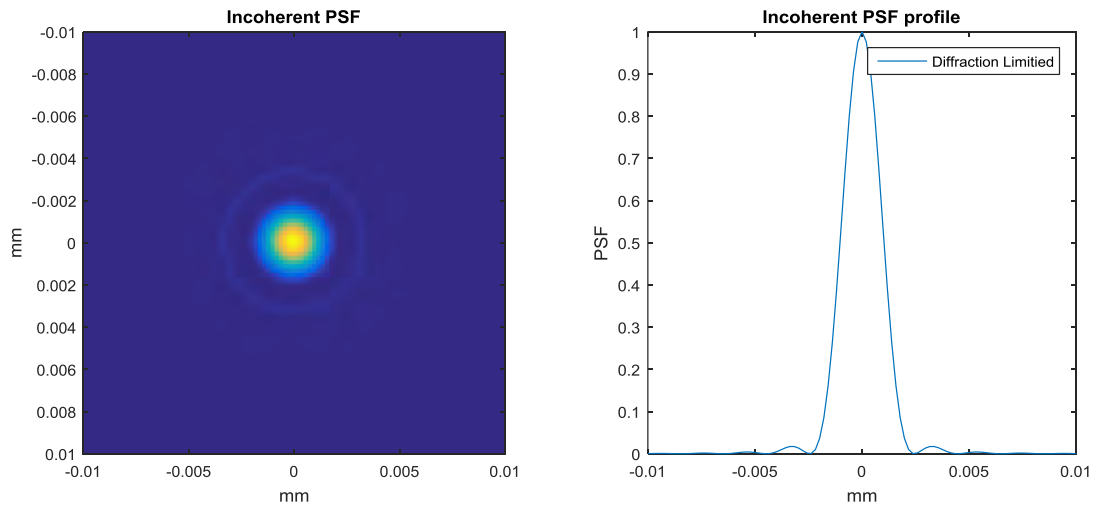


Figure 2.1) Incoherent Point Spread Function for a diffraction limited system (Left); also known as the Airy disk. Line Profile of the same function (Right)

Another useful metric to verify is the cutoff frequency. The cutoff frequency is where the MTF goes to zero, and can be calculated in cycles per mm as follows:

$$f_{cutoff} = \frac{1}{\lambda F/\#} [\text{cyc/mm}] \quad (2.2)$$

$$f_{cutoff} = \frac{1}{\lambda F/\#} \frac{\pi}{180} z_{xp} [\text{cyc/degree}] \quad (2.3)$$

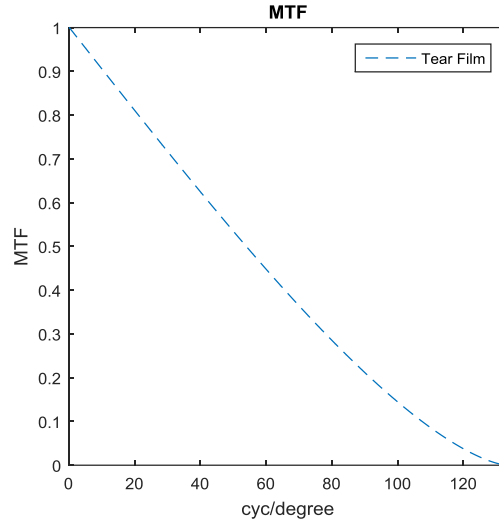


Figure 2.2) MTF for a diffraction limited system

Using MATLAB software to determine exact values from the plots above, the measured values were compared to theoretical ones in the table below:

Table 2-2) Results of analysis on a diffraction limited system with TFI analysis software

	Theoretical	Measured	% Error
Airy Disk diameter (μm)	4.88	4.75	2.63
Cutoff Frequency (cyc/degree)	133.43	133.36	0.05

The error in the diameter of the Airy disk is likely due to the discrete nature of the DFT.

2.2 SEIDEL ABERRATIONS

The next step of verification was to analyze the system with more complicated wavefront shapes. The Seidel wavefront polynomial provides wavefront sag profiles whose behavior in optical systems are well known. Existing literature provides sample code that performs the same kind of Fourier analysis on wavefronts (Voelz, 2011). The Seidel wavefront coefficients are available as inputs for Voelz's code.

The PSF shape caused by 1λ of defocus is well known, and was tested with both sets of code.

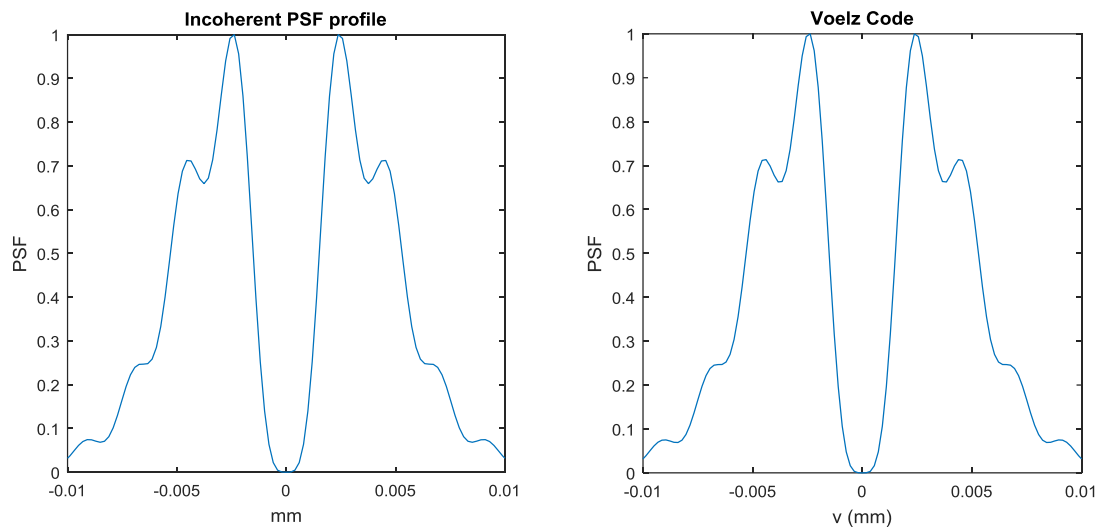


Figure 2.3) 1λ of W020 results in a well-known PSF pattern, shown in both TFI analysis software (Left) and Voelz's code (Right)

The two sets agree. Now that any Seidel wavefront shape could be analyzed by the system, the next step was to determine PSF, MTF and SQF measurements for the different eye models that are going to be applied to the tear film. Two eye models were chosen as the basis for this analysis: the Arizona

Eye Model and the Typical Human Eye Aberration Model. They are described in the following sections.

The analysis in Section 1 has been implemented in MATLAB code to produce the PSF, MTF and SQF based upon the tear film wavefront error in the entrance pupil of the eye. This wavefront error is scaled (resized) to the exit pupil of the eye. An eye model is used to generate the inherent aberrations of the eye and give this wavefront error in the exit pupil of the eye. The wavefront errors due to the measured tear film are added to the modeled eye wavefront aberration. This net wavefront aberration is used in the calculation of the system MTF, PSF and SQF.

2.3 EYE MODELS

2.3.1 ARIZONA EYE MODEL

Dr. Schwiegerling's Arizona Eye Model (AZEM) has a ZEMAX file publicly available online for download. By exporting the Wavefront OPD in the pupil into an excel file, this array can easily be imported into MATLAB and analyzed by the software. The wavefront sag in the pupil of the AZEM is shown below. There is a maximum wavefront error due to spherical aberration of about 2 waves (P-V). This error is not corrected for best focus.

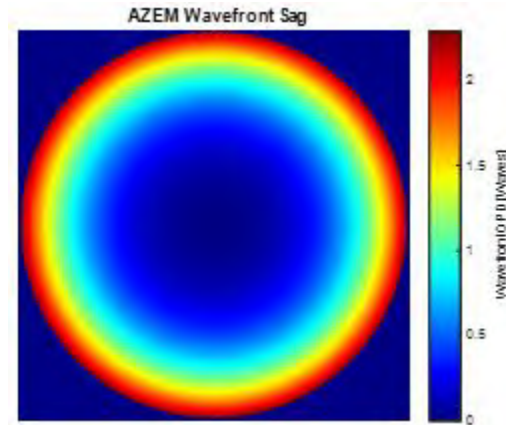


Figure 2.4) AZEM wavefront OPD in pupil (4.5 mm Pupil Diameter)

2.3.2 TYPICAL HUMAN EYE ABERRATION MODEL

Rather than using an eye model, a simpler approach is to merely use an equation describing the power distribution or aberrations of the eye.

An equation for aberrational eye power is described by Equation 2.4, and the equation for wavefront error (Equation 2.8) was derived from this. It will be referred to as the Typical Human (TH) Eye Aberration Model. This function is corrected with defocus (mid-focus) for the best image plane. Figure 2.5 shows a 2D plot of the function derived in Equation 2.8. AD is the maximum entrance pupil or analysis diameter and r is the radial position in the pupil (both in mm).

$$P = (0.08D/mm^2) r^2 - 0.5(0.08D/mm^2) \left(\frac{AD}{2}\right)^2 \quad [\text{diopters}]$$

(2.4)

Equation 2.4 shows the aberrational power as measured in diopters. This corresponds to spherical aberration, and the values were suggested by the research sponsor. The scalar values in the equation have units of diopters per millimeters squared. The radius variable, or r , is given in millimeters. The variable is squared and so the millimeters cancel, leaving only units of diopters.

$$P = \frac{1}{r} \frac{dW}{dr} \text{ [diopters]} \quad (2.5)$$

Equation 2.5 allows power and wavefront error to be related.

$$\frac{dW}{dr} = (.08D/mm^2)r^3 - \frac{.05(.08D/mm^2)}{4}(AD^2 * r) \text{ [diopter mm]} \quad (2.6)$$

Equation 2.5 was solved for by setting Equations 2.4 and 2.5 equal to each other and solving for the derivative of wavefront error with respect to radius. The extra radial term changes the units to diopter millimeters.

$$W = \int \frac{dW}{dr} dr \text{ [diopter } mm^2\text{]} \quad (2.7)$$

Equation 2.7 shows how to calculate wavefront error from Equation 2.6. The integral is with respect to radius, which is measured in millimeters. This gives the wavefront (W) units of diopter mm squared. This is an uncomfortable unit, so the expression will be scaled by .001 converting the diopters into inverse millimeters. This makes the expression millimeters squared per millimeter. One of the millimeters in the numerator now can cancel with the term in the denominator, resulting in

only units of millimeters. Equation 2.7 also divides by wavelength to convert to units of waves.

$$W = \frac{1e^{-3}}{\lambda} \int \frac{dW}{dr} dr \text{ [waves]} \quad (2.8)$$

$$W = \frac{1e^{-3}}{\lambda} \frac{r^2}{50} \left(r^2 - \frac{AD^2}{4} \right) \text{ [waves]} \quad (2.9)$$

Equation 2.8 is the result of plugging Equation 2.6 into Equation 2.7 and solving the integral. This expression will define the wavefront error for the TH aberrational model. This eye model is the basis for the SQF values in the results section.

Evaluating the first half of Equation 2.9, isolating the spherical aberration content only, yields about 0.1 waves of Spherical Aberration (P-V).

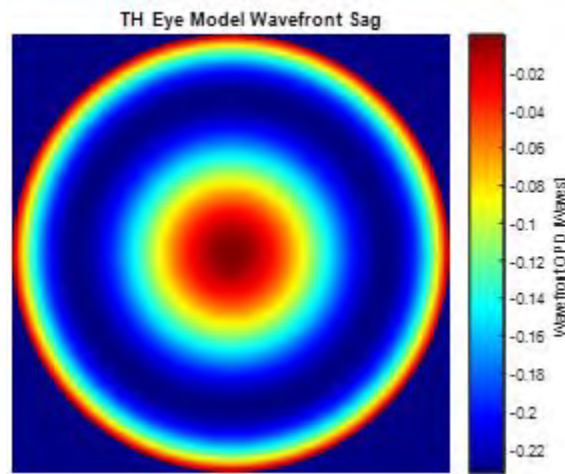


Figure 2.5) Typical Human Eye Aberration Model wavefront OPD in pupil (4.5 mm Pupil Diameter)

The peak to valley measurements vary significantly between the two models, and so an additional resource was considered for comparison. In a 2001 study, the mean Zernike coefficients for a 5.7 mm pupil were determined across 109 subjects (Porter et al., 2001). The pupil diameter for the two

previous models was adjusted from 4.5mm to 5.7mm to match the resource, and the Z40 RMS values were compared between the three. The Z40 TH value was found by performing a Zernike fit. This was done by setting Equation 2.9 equal to a Z40 Zernike polynomial and solving for the coefficient. The piston term is ignored since that value will be irrelevant for the RMS calculation.

$$1e^{-3} \frac{r^2}{50} \left(r^2 - \frac{AD^2}{4} \right) = \frac{a_{40}(6\sqrt{5})}{r_{max}^4} (r^4 - r^2 r_{max}^2) \quad (2.10)$$

$$a_{40} = \frac{r_{max}^4}{300\sqrt{5}} 1e^{-3} \quad (2.11)$$

$$a_{40} = .098 \mu m \quad (2.12)$$

As expected, the plots for the TH aberration eye model matches its Zernike fit almost perfectly.

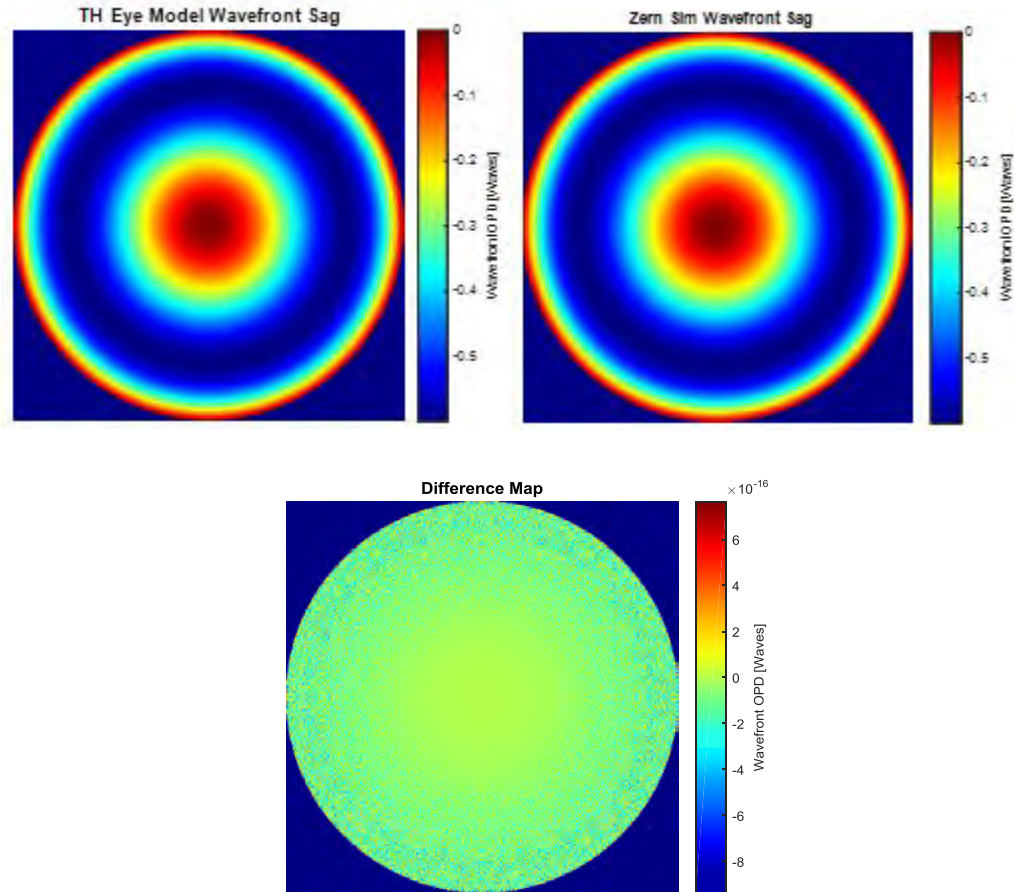


Figure 2.6) The TH model wavefront (Left), the Zernike fit (Right), and the difference between the two (Bottom) (5.7 mm Pupil Diameter)

Table 2-3) Z40 coefficient results for different eye models at a 5.7 mm pupil diameter

Eye Model	Z40 RMS (μm)
Typical Human	0.098
Porter	0.15

The Z40 content for the Typical Human aberration model matches this published data and the TH model will be used for this analysis. It should be noted that it appears that the AZEM contains significantly more Spherical Aberration than the TH model.

2.4 THE TEAR FILM

2.4.1 WAVEFRONT SCALING

The final step in the verification process is to add the tear film. The purpose of this report is to analyze the change in visual quality produced by the tear film, and the verification of simpler systems has led to this final step of added complexity.

The first step in that use of the TFI data is to window it to the diameter of the entrance pupil. As noted earlier, all of the analysis to date uses a 4.5 mm diameter entrance pupil. This is shown in Figure 2.7.

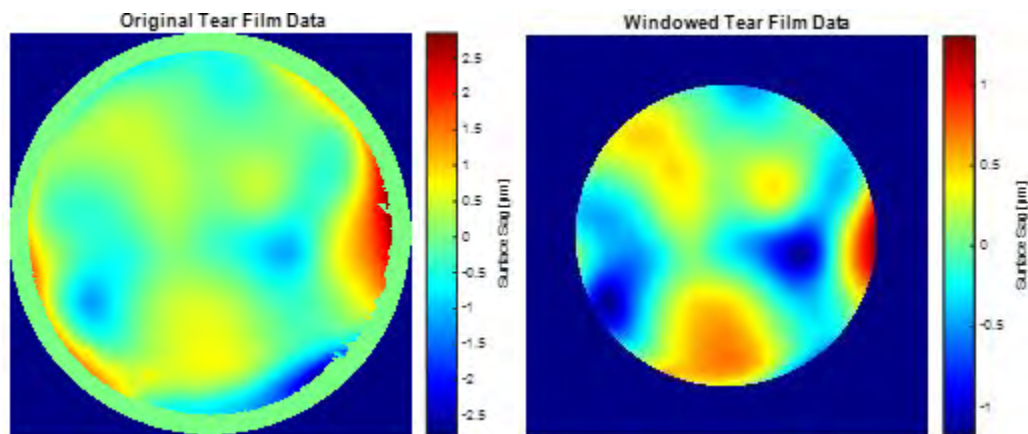


Figure 2.7) Tear Film data produced by the TFI (Left) (6.0 mm Pupil Diameter), windowed down (Right) (4.5 mm Pupil Diameter)

This windowed surface needs to be converted to transmitted wavefront and eventually phase for the new TFI analysis software. The TFI height data is multiplied by $(n_{\text{tear film}} - 1)$ to get the OPD. This

value is divided by the wavelength to convert to waves of OPD or wavefront error. The index of the vitreous was used as the index of the tear film.

This wavefront map must now be translated to the exit pupil of the eye. This is done by lateral scaling by the entrance pupil to exit pupil magnification. A 4.5 mm entrance pupil produces a 4.2 mm exit pupil in the AZEM.

To verify that the OPD of the surface was being correctly calculated, the output of the TFI software was compared to a raytrace analysis of the AZEM using Zemax. For proper comparison, the wavefront error produced by the AZEM was used for the TFI analysis.

The tear film data was imported into ZEMAX as a grid sag on the cornea of the model. This requires changing the surface type from *Standard* to *Grid Sag* in ZEMAX. The AZEM wavefront error is shown in Figure 2.8 - Left. The addition of the tear film onto the cornea in the AZEM produces the wavefront error shown in Figure 2.8 - Right.

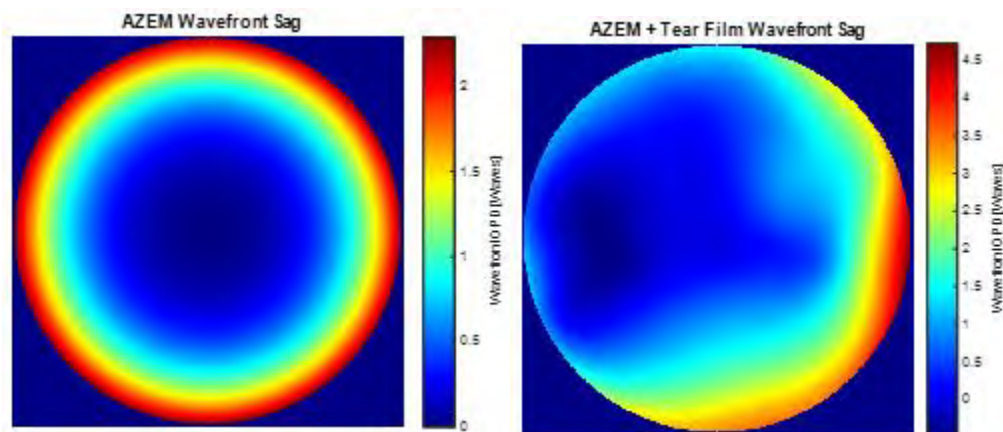


Figure 2.8) Arizona Eye Model wavefront OPD for two different corneal topographies, without (Left) and with the tear film (Right) (4.5 mm Pupil Diameter)

Wavefront errors sum. Therefore, the two figures above can be subtracted from one another, and the residual wavefront error (WFE) is caused only by the tear film. This is better described by Equations 2.11 and 2.12 below. $WFE_{AZEM+TEARFILM}$ is the WFE in the pupil for the AZEM with the tear film applied. WFE_{AZEM} is the WFE in the pupil for only the AZEM (no tear film). $WFE_{TEARFILM}$ is then the remaining WFE in the pupil that is caused by the tear film. Equation 2.13 can be rearranged to solve for this WFE that is caused by the tear film (Equation 2.14).

$$WFE_{AZEM+TEARFILM} = WFE_{AZEM} + WFE_{TEARFILM} \quad (2.13)$$

$$WFE_{TEARFILM} = WFE_{AZEM+TEARFILM} - WFE_{AZEM} \quad (2.14)$$

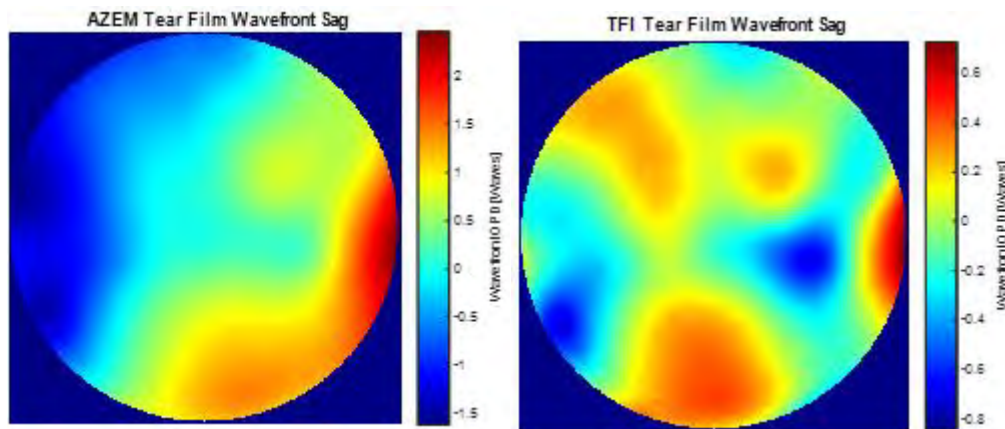


Figure 2.9) Tear film wavefront OPD from residual AZEM (Left) and from TFI (Right) (4.5 mm Pupil Diameter)

The figure on the left (Figure 2.9) shows the tear film WFE calculated using Equation 2.13. The figure on the right is simply the windowed tear film data produced by the TFI (Figure 2.7 - Right), but in the pupil, where it has been scaled by the index change and displayed in units of waves. These two graphs should match, but there is apparent tilt between the two plots. This is likely due to a decentration of the grid sag surface on the Zemax implementation. To investigate further, a residual difference was calculated (Figure 2.10 – Left).

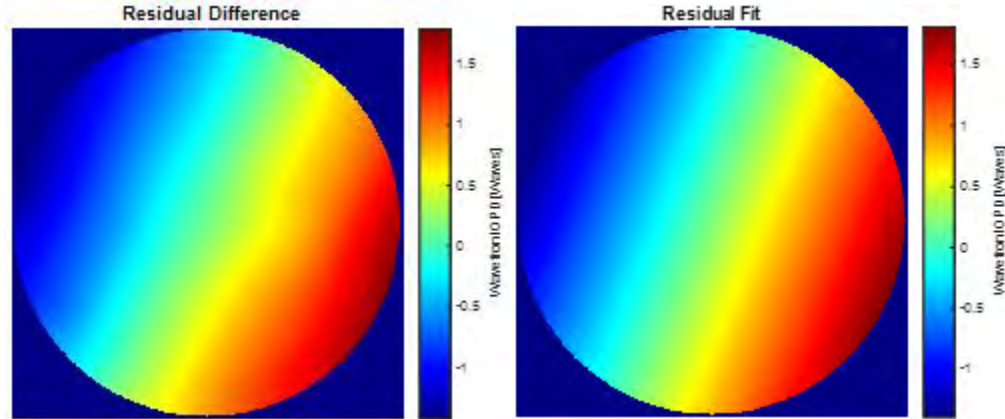


Figure 2.10) Differences in the two Figure 2.9 wavefront OPDs (Left) and a residual fit (Right) (4.5 mm Pupil Diameter)

Figure 2.10 clearly shows that the difference between the two wavefront sags is only tilt. The figure on the right is a residual fit simulated in MATLAB so that this tilt term can be subtracted. This fit can then be removed from the AZEM Tear Film (Figure 2.9 - Left). This produces the left plot in Figure 2.11. The TFI tear film wavefront sag (Figure 2.11 - Right) is shown again for comparison.

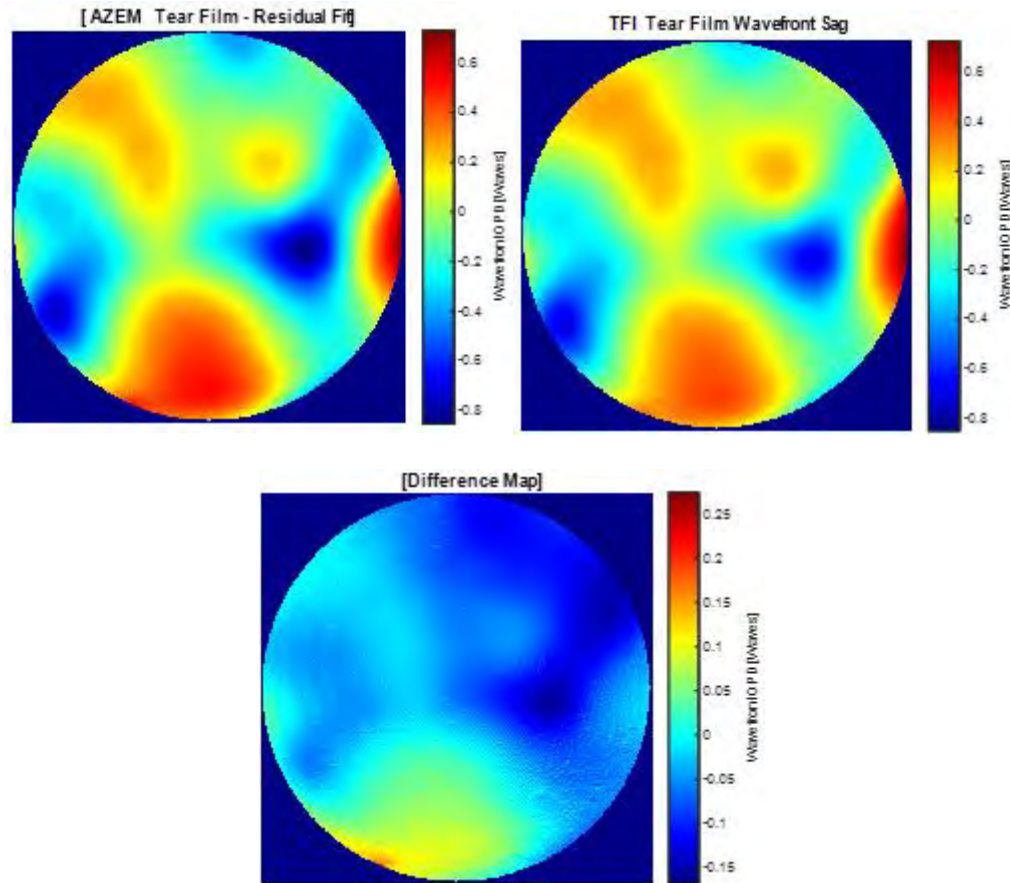


Figure 2.11) AZEM tear film wavefront OPD (Left), the TFI tear film wavefront OPD (Right), and the difference (Bottom) (4.5 mm Pupil Diameter)

The PV error of this difference map (Figure 2.11 - Bottom) provides confidence that the index change OPD associated with the tear film is being calculated correctly. This conversion between surface height and wavefront has been properly implemented.

2.4.2 THE INCOHERENT PSF

Now that the OPD in the pupil is verified, the DFT analysis needs to be checked against ZEMAX FFT PSF analysis as well. To make sure the new TFI analysis software is working as it should, the TFI

output PSF will be compared to the ZEMAX output PSF. Both of the plots below were produced using the same WFE in the pupil.

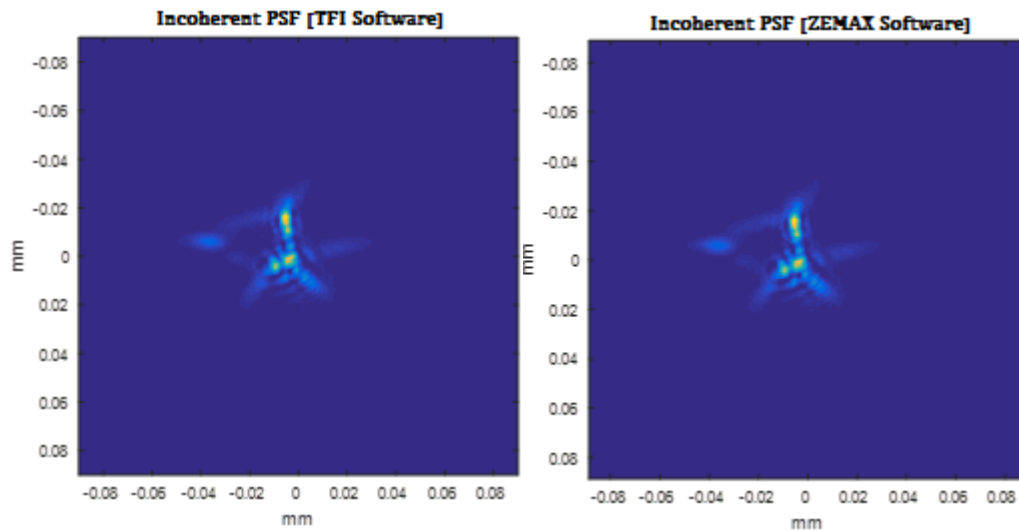


Figure 2.12) The incoherent produced by the TFI Software (Left) and the one produced by ZEMAX FFT software (Right).

The PSF of the new TFI analysis software and ZEMAX match quite well. The features are remarkably consistent and the scales agree as well.

2.4.3 THE MODULATION TRANSFER FUNCTION

In accordance with the theory described in Section 1, the MTF was calculated from the incoherent PSF with Fourier theory calculations. Referring back to Equation 1.15, the SQF is calculated as the area under an MTF cross section between two spatial frequency limits. The spatial frequency limits chosen for visual quality analysis were 3 cycles/mm and 18 cycles/mm. Figure 2.13 shows the four different MTF meridionals that were used for analysis. The cuts occur at 0, 45, 90 and 135 degrees. MTFs are symmetric about zero, so only half of the spatial frequency were used to plot the MTF

cross sections. This is proven in a quick derivation below.

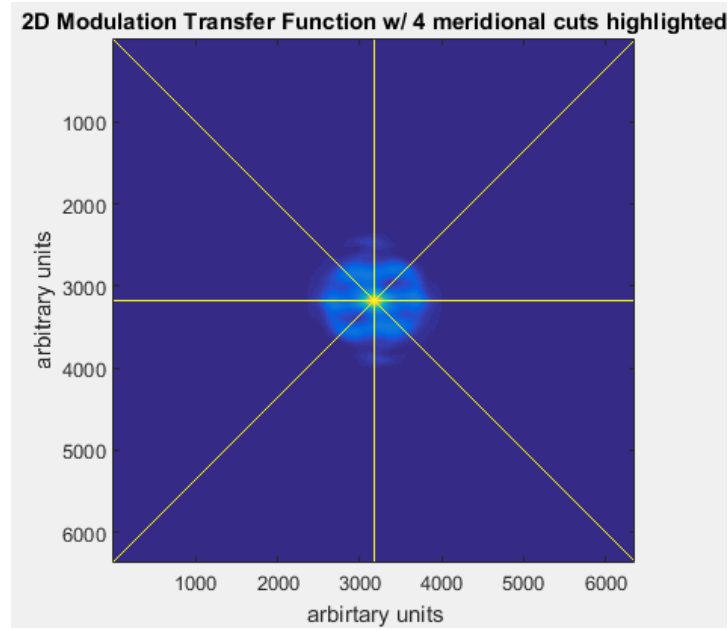


Figure 2.13) The MTF is related to the Fourier transform of the incoherent PSF

Equation 1.14 can be restated as

$$MTF \propto \int_{-\infty}^{\infty} PSF_{incoherent}(x) e^{-j2\pi\xi x} dx \int_{-\infty}^{\infty} PSF_{incoherent}(x) e^{+j2\pi\xi x} dx \quad (2.15)$$

Any function can be split into its real (u) and imaginary terms (v).

$$PSF_{incoherent} = u(x) + jv(x) \quad (2.16)$$

$$MTF \propto \int_{-\infty}^{\infty} (u(x) + jv(x))e^{-j2\pi\xi x} dx \int_{-\infty}^{\infty} (u + jv(x))e^{+j2\pi\xi x} dx \quad (2.17)$$

The incoherent PSF is a completely real term, since it was calculated using a magnitude operation.

This operation was shown in Equation 1.12. This means $v(x) = 0$, resulting in Equation 2.18.

$$MTF \propto \int_{-\infty}^{\infty} u(x)e^{-j2\pi\xi x} dx \int_{-\infty}^{\infty} u(x)e^{+j2\pi\xi x} dx \quad (2.18)$$

Any function can be split up into the sum an odd function and an even function.

$$u(x) = u_o(x) + u_e(x) \quad (2.19)$$

The exponential functions can be redefined in terms of sines and cosines per Euler's formula.

$$e^{-j2\pi\xi x} = \cos(2\pi\xi x) + j\sin(2\pi\xi x) \quad (2.20)$$

Combining these two equations yields the following.

$$MTF \propto \int_{-\infty}^{\infty} [u_o(x) + u_e(x)][\cos(2\pi\xi x) - j\sin(2\pi\xi x)] dx \times \int_{-\infty}^{\infty} [u_o(x) + u_e(x)][\cos(2\pi\xi x) + j\sin(2\pi\xi x)] dx \quad (2.21)$$

$$\begin{aligned}
 & \int_{-\infty}^{\infty} \left[\begin{array}{c} u_o(x) \cos(2\pi\xi x) - j u_o(x) \sin(2\pi\xi x) \\ + \\ u_e(x) \cos(2\pi\xi x) - j u_e(x) \sin(2\pi\xi x) \end{array} \right] dx \\
 & \qquad \qquad \qquad \times \\
 MTF \propto & \int_{-\infty}^{\infty} \left[\begin{array}{c} u_o(x) \cos(2\pi\xi x) + j u_o(x) \sin(2\pi\xi x) \\ + \\ u_e(x) \cos(2\pi\xi x) + j u_e(x) \sin(2\pi\xi x) \end{array} \right] dx
 \end{aligned} \tag{2.22}$$

Table 2-4) Function handedness properties

Function 1 Handedness	Function 2 Handedness	Operation	Resulting Function Handedness
odd	odd	×	even
even	even	×	even
odd	even	×	odd
even	even	+	even

The integral over an odd function for infinite bounds is always zero. Cosine functions are even, and sine functions are odd. Equation 2.22 can then be reduced so only even functions remain.

$$\begin{aligned}
 & \int_{-\infty}^{\infty} [-j u_o(x) \sin(2\pi\xi x) + u_e(x) \cos(2\pi\xi x)] dx \\
 & \qquad \qquad \qquad \times \\
 MTF \propto & \int_{-\infty}^{\infty} [j u_o(x) \sin(2\pi\xi x) + u_e(x) \cos(2\pi\xi x)] dx
 \end{aligned} \tag{2.23}$$

Equation 2.23 shows the product of two integrals of even functions. The integral of an even function is always odd. This means this equation shows the product of two odd functions. As stated earlier in Table 2.4, the product of two odd functions is an even function. Nothing else is left to be reduced. This proof shows that the MTF will always be even, and only examining the positive spatial frequencies is now justified.

The SQF calculation will not be explored any further. It is straightforward and was already described in Section 1.4, specifically Equation 1.15.

This is the final step in verification. The analysis software and eye models have been verified and checked in several different ways, which gives confidence for this analysis to move forward towards results.

In the results, a single horizontal meridian cross section will be taken from the 2D incoherent PSF to more easily compare it against the TH aberration eye model PSF.

3.0 ANALYSIS SOFTWARE

Automation software for tear film analysis was a large portion of this project. In this section the software's capabilities are explained.

The TFI analysis software is split into two distinct parts. The first script is the Movie software, which performs the Fourier analysis on the tear film, and calculates the corresponding visual quality metrics, including the SQF. It then creates a movie file where the tear film wavefront, 2D incoherent

PSF, an incoherent PSF line profile, and 4 MTF line profiles are shown changing over time for the entirety of the collect.

The second script is the Post Processing code. This code plots the calculated SQF values from before and provides options to filter out noisy values, producing a filtered SQF chart and a filtered movie.

3.1 MOVIE SOFTWARE

Analysis software has been written that processes tear film data. The original program was built to analyze ICT data. The user GUI for this software makes it possible to set several initial conditions for the Fourier analysis. These possible conditions are set using the GUI shown in Figure 3.1 below.

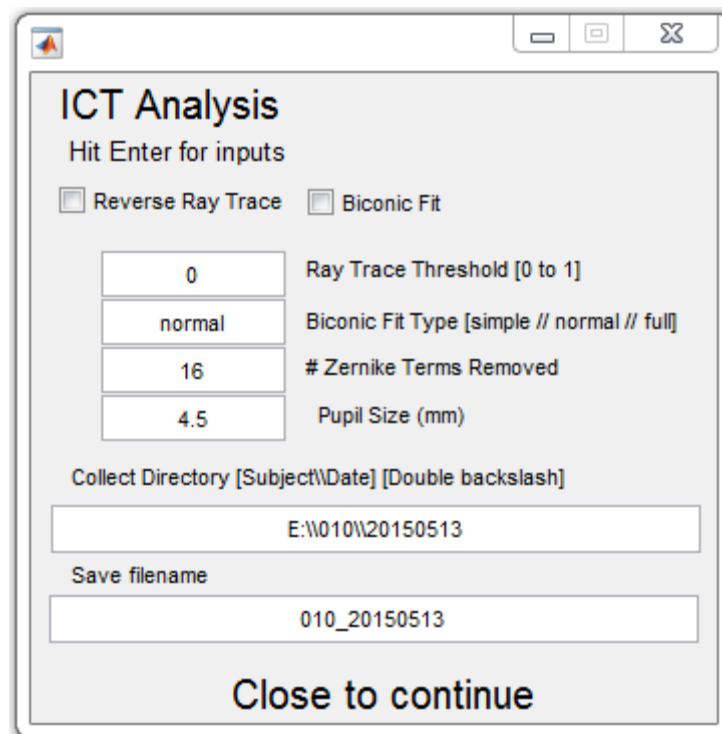


Figure 3.1) Analysis GUI for TFI data

As shown above, reverse ray tracing and a biconic fit removal are possible for ICT data. The Ray Trace Threshold condition refers to a filter based on the fraction of rays successfully reverse ray traced through the system allows for some pre-processing filtering. If the reverse ray tracing code does not satisfy the threshold, the program skips the Fourier analysis code and sets the surface height map to a uniform zero. This saves some processing time, which is the motivation for making this threshold a preprocessing filter rather than making it apart of the post processing script. These zero frames carry no meaningful information, and can be easily filtered out later with the post processing script.

When the biconic removal and reverse ray tracing options are left unchecked, the ICT becomes a functional TFI, which was described in section 1.1.2.

A Zernike fit removal of up to 99 terms can be performed on the data. The pupil size can be windowed to anything less than the original data size of 6 mm.

The output of this movie software is shown in Figure 3.2. The tear film wavefront first shown in Figure 2.7 is in the upper left hand corner. The incoherent point-spread function shown in Figure 2.12 is displayed in the upper right hand corner. The lower left hand corner is a horizontal line profile at 0 degrees through the incoherent point-spread function. This is typically how point spread functions are viewed and also provides a comparison with the TH aberration eye model. Finally the lower right-hand corner compares the MTF of TH aberration eye model with the four line profiles of the tear film and MTF. These are the four cross-sections that were described in Section 2.4.3.

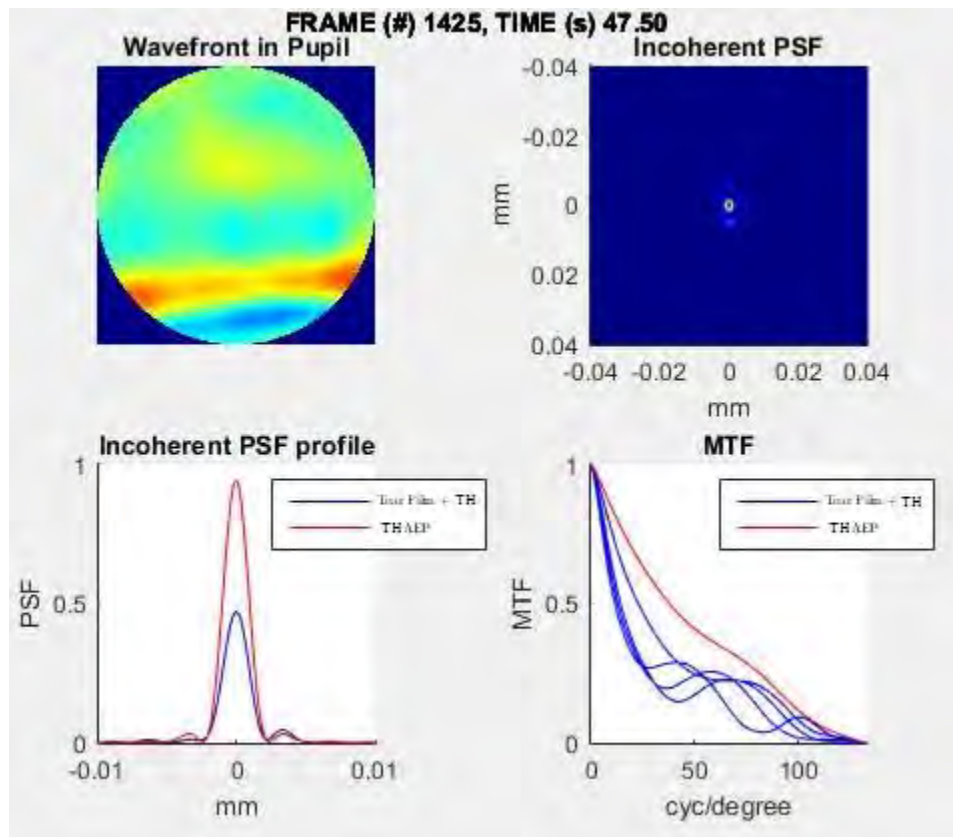


Figure 3.2) Single frame snapshot of the visual quality movie

The TFI movie file naming convention is formatted such that it contains all the relevant information about the collect.

3.2 POST PROCESSING SOFTWARE

This is a necessary part of the process due to the frequent occurrence of noisy data, or bad frames. The post processing code allows the user to vary several initial conditions with the goal of filtering out the bad frames.. The Movie software code saves all the necessary information in one matrix.

When the Post Processing software is executed, this matrix needs to be loaded into the workspace.

This is accomplished with the GUI shown in Figure 3.3.

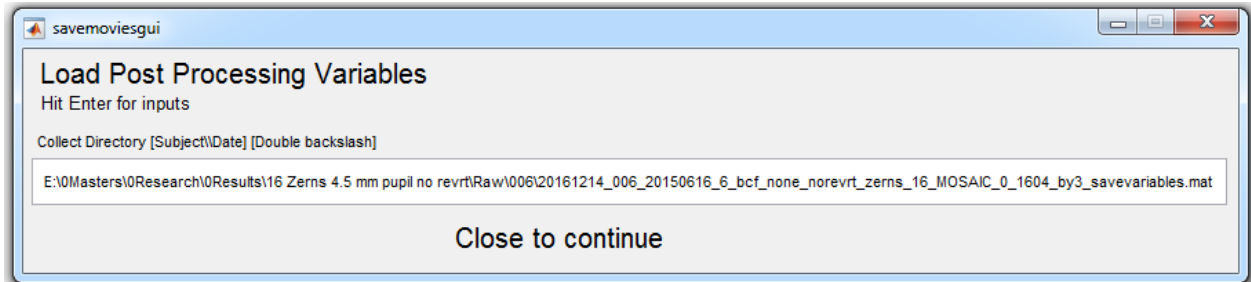


Figure 3.3) Load post processing variables GUI

The post processing GUI is shown in Figure 3.4 below.

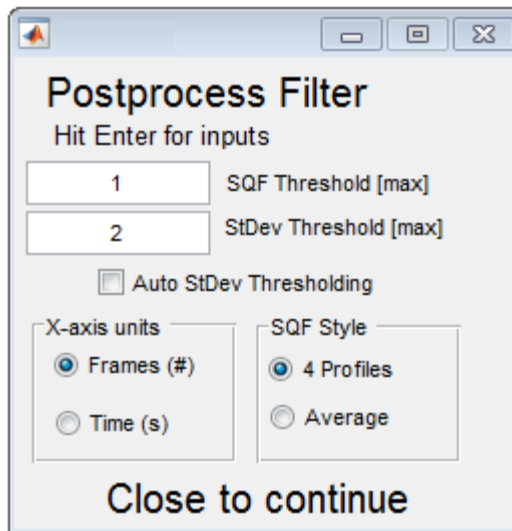


Figure 3.4) Post-processing GUI

Filtering options and display options both exist in this GUI. The filtering options will be covered first.

3.2.1 SQF FILTER

The SQF threshold refers to the maximum threshold change in cyc/mm between adjacent frames before the data is discarded. For the setting shown in Figure 3.4, if the change between adjacent SQF values exceeds 1, the second data point is discarded.

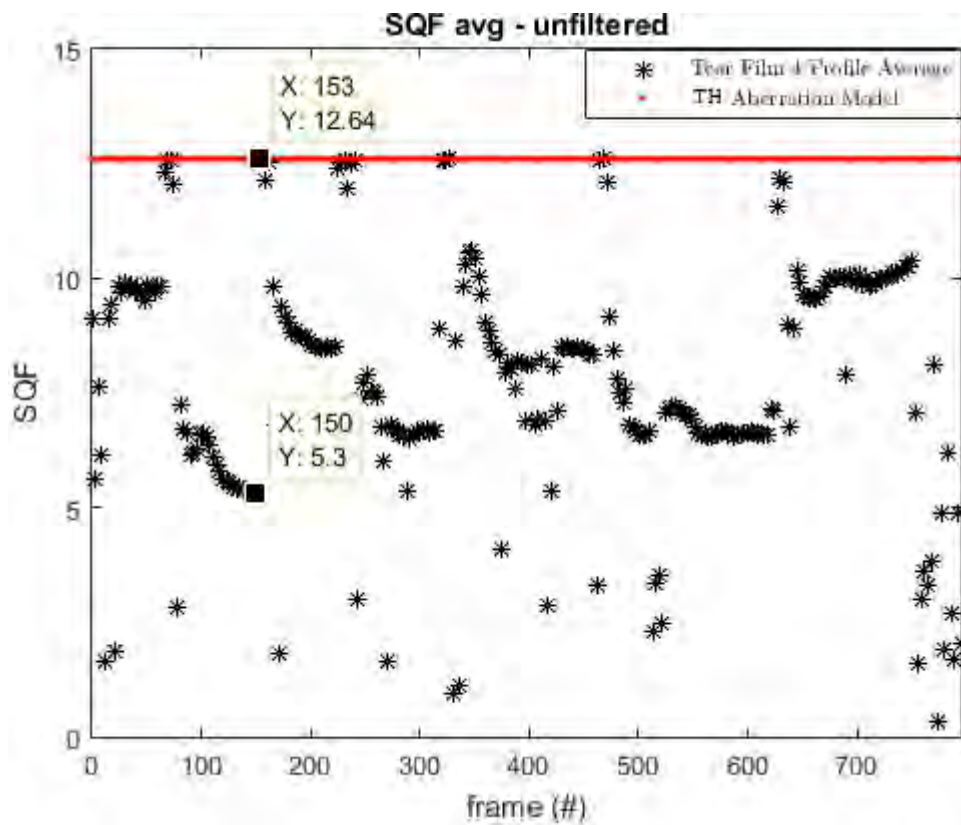


Figure 3.5) SQF (average) chart [frames 150 and 153 highlighted]

Figure 3.5 shows the SQF values for two adjacent points. The initial collects were 30 FPS, and then downsampled to 10 FPS, so adjacent points are separated by 3 frames. The differential between

these two points is approximately 7 cyc/mm, which far exceeds the set SQF threshold of 1 cyc/mm shown in Figure 3.4. This means frame 153 will be filtered out.

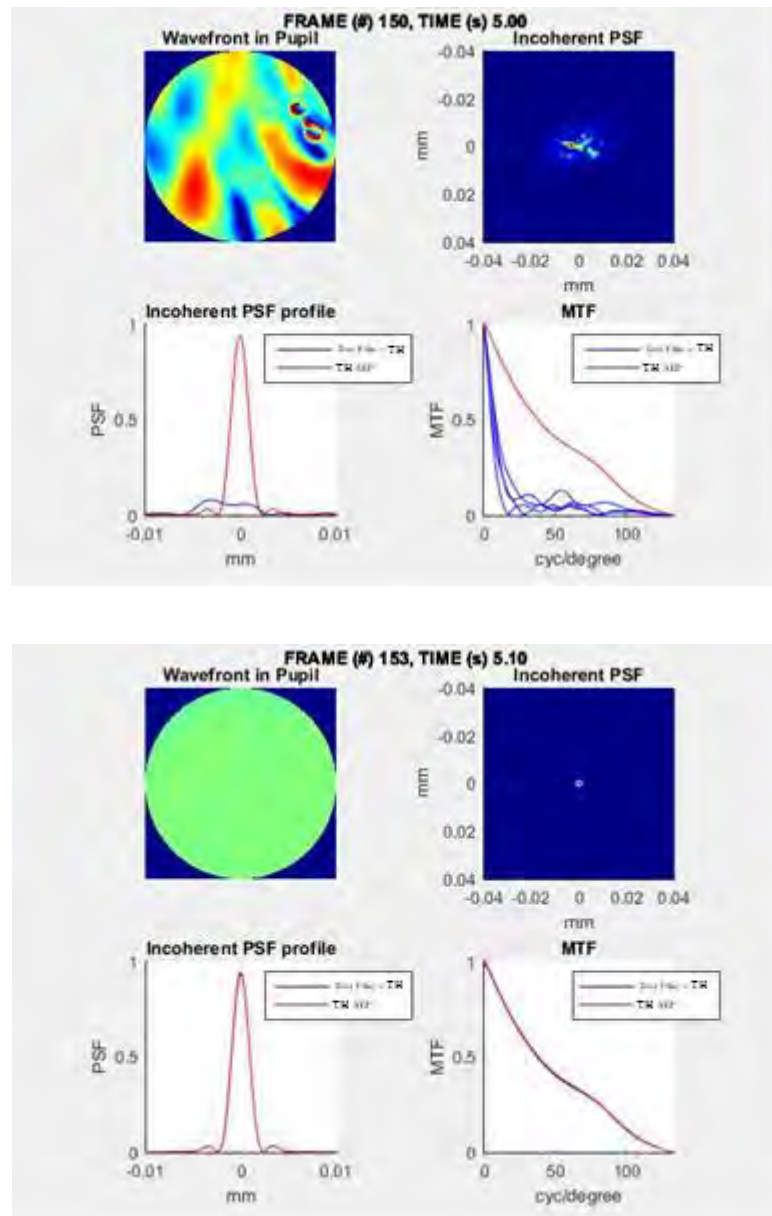


Figure 3.6) Movie Snapshots for frames 150 (top) and 153 (bottom) shown in Figure 3.5

Figure 3.6 shows the movie snapshots associated with those particular frames. The tear film changed so rapidly that it is unlikely that frame 153 contains useful information. In the figure it is clear that frame 153 shows almost no tear film deformation, which is extremely unlikely given the

context of the collect. The video indicates that the subject began a blink around frame 153, so the SQF value associated with frame 153 carries no meaningful information.

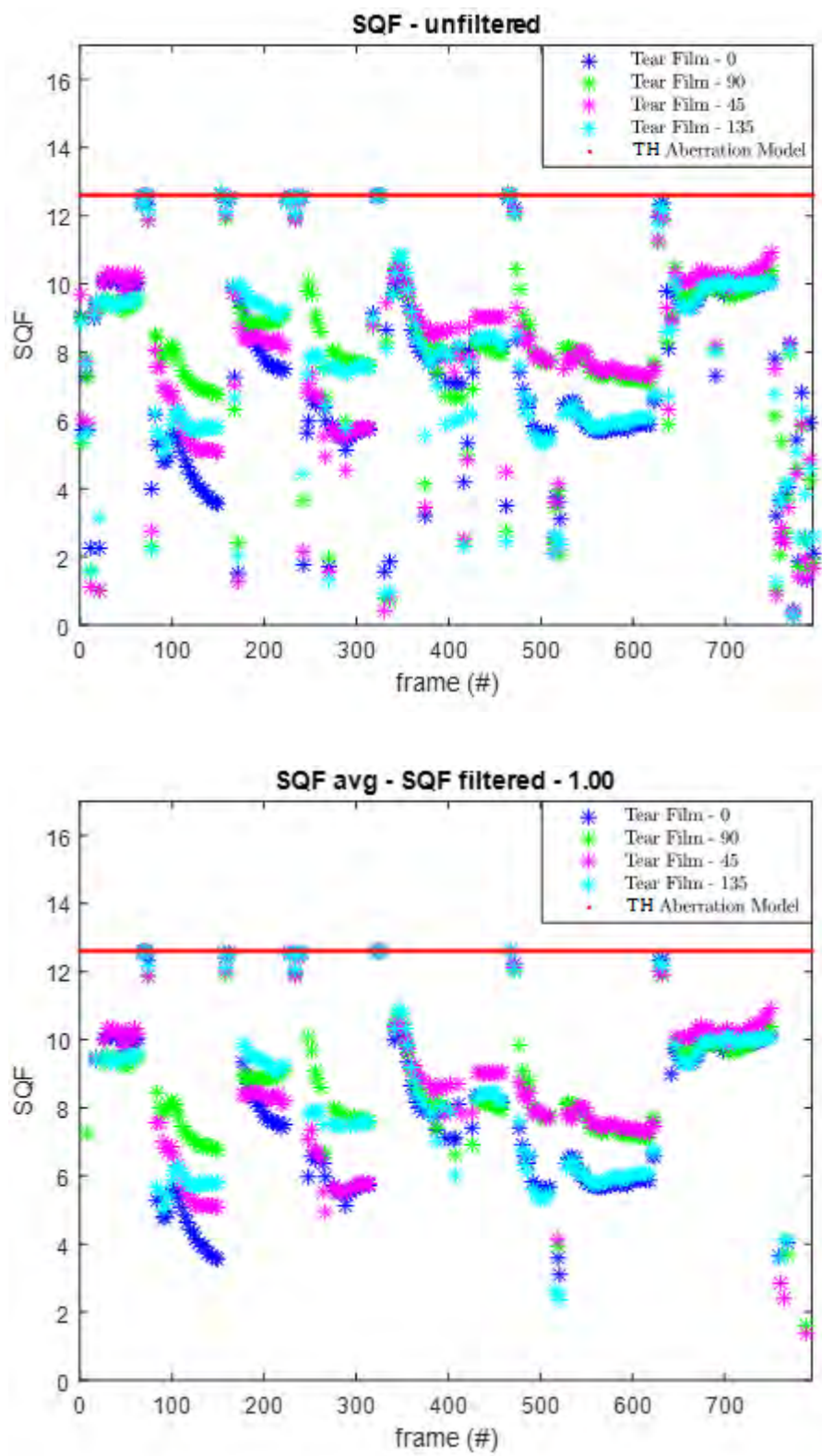


Figure 3.7) SQF charts, with (bottom) and without (top) SQF filtering

Figure 3.7 shows the utility of this filter. The continuous parts of the data run are left untouched, and much of the noise has been filtered out.

This method has a couple flaws. First, these tear film data sets usually come through processing as a continuous run of good frames followed by a run of noisy frames. So in the case of a continuous run of good frames, the first frame will be filtered out, due to the filtering process cutting out the second data point. Since the TFI collects thousands of frames, a few lost frames was determined to be acceptable.

Another issue is that the software doesn't know the difference between a continuous run of good frames and a continuous run of bad frames. It is for this reason that the SQF threshold filter is better at filtering out scattered noise rather than contiguous points. A possible solution to this issue could be to run the SQF filter multiple times. This was determined to be a poor solution due to the lost frames limitation stated above.

This method does not check for the integrity of the data set's first point. Should the differential between the first pair of adjacent points fail the threshold, both will be thrown out. If it doesn't, both will be kept. So this problem is mitigated by this new condition.

Rare data sets can also cause issues with this algorithm. If a data set never has a continuous run of good frames, but rather every other frame is considered good signal, every frame will be filtered out. In this case the SQF threshold would need to be lowered or set to zero and the Standard Deviation (StDev) threshold in the next section would become the more useful tool. Most of the TFI data sets did not show this on/off behavior so this was never an issue.

3.2.2 STANDARD DEVIATION FILTER

These limitations create a need for a different type of filter. A standard deviation filter was chosen to filter out the remaining bad frames. Standard deviation is a useful one number metric that describes the variance of the height map across the frame, as well as the variance of these values across a collect. The expression for standard deviation is shown below in Equation 3.1.

$$\sigma_{frame} = \sqrt{\frac{1}{N_{pixels}} \sum_{i=1}^{N_{pixels}} (x_i - \mu)^2} \text{ where } \mu = \frac{1}{N} \sum_{i=1}^N x_i \quad (3.1)$$

The σ_{frame} is the standard deviation of the frame, where all the x values represent the pixelated height map values from the tear film wavefront, N represents the total number of pixels, and μ is the average height for all pixels.

The user input StDev threshold (shown in Figure 3.4), put simply, is a standard deviation of a standard deviation. The code calculates the σ_{frame} for each frame for the entire collect. Although the code produces no such figure, the graph displaying this is shown below in Figure 3.8 for understanding.

The outlier in the following plot skews the scale so drastically that it appears there is no variation in the σ_{frame} value across the set. This is not the case, as can be seen in the following figures after the outlier is filtered out. Typical values for σ_{frame} is less than 0.1 mm.

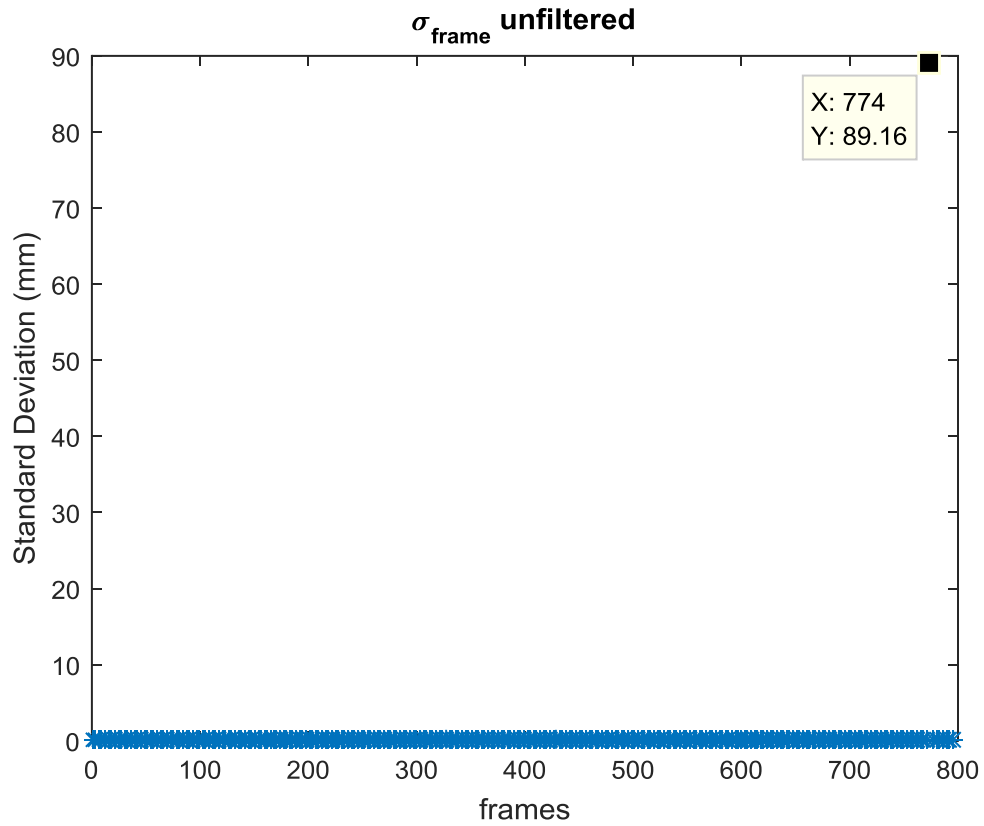


Figure 3.8) Standard Deviation for each frame over entire collect - unfiltered

Immediately, it is clear that there is an outlier in the upper right hand corner of Figure 3.8. This value occurs at frame 774. Since it is extremely unlikely that the standard deviation has changed that drastically, the StDev will attempt to filter this point out, if provided with a reasonable user input value.

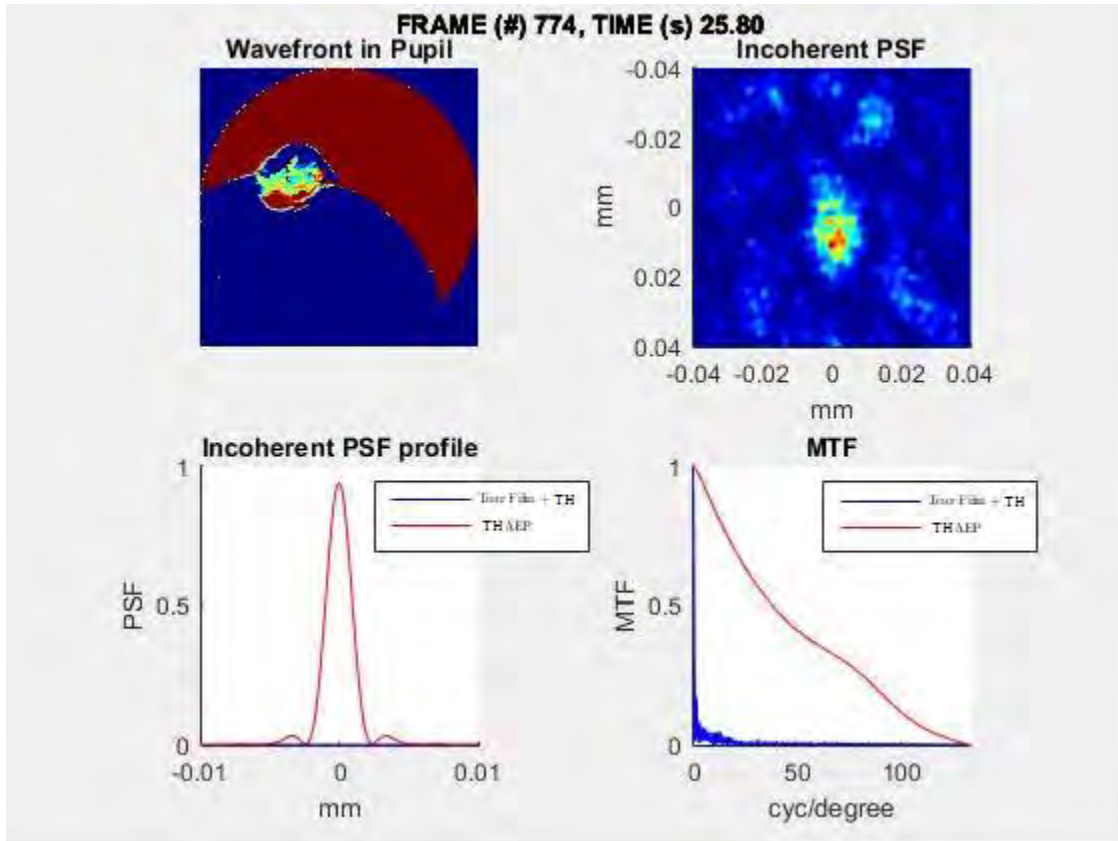


Figure 3.9) Movie snapshot for frame 774 highlighted in Figure 3.8

The drastic shape of the tear film in frame 774 confirms that this frame needs to be filtered out for data integrity.

The standard deviation filter again uses Equation 3.1, except now the x values represent the σ_{frame} value, N represents the total number of frames in the collect, and μ is the average σ_{frame} for all frames.

$$\sigma_{threshold} = \sqrt{\frac{1}{N_{frames}} \sum_{i=1}^{N_{frames}} (\sigma_{frame} - \mu)^2} \text{ where } \mu = \frac{1}{N} \sum_{i=1}^N \sigma_{frame} \quad (3.2)$$

The StDev Threshold value from Figure 3.4 will act as a multiplier on this $\sigma_{threshold}$ value, and filter out all σ_{frame} values that are outside of this threshold. Equation 3.3 describes the filtering operation. In this example the StDev Threshold value was set to 2.

$$\begin{aligned}
 & \text{if } 2 \times \sigma_{threshold} > \sigma_{frame} \\
 & \sigma_{frame} = 0
 \end{aligned}
 \tag{3.3}$$

Any σ_{frame} that is 2 standard deviations outside the average will be filtered out. This operation was performed on the data set, and the data in Figure 3.8 turns into Figure 3.10.

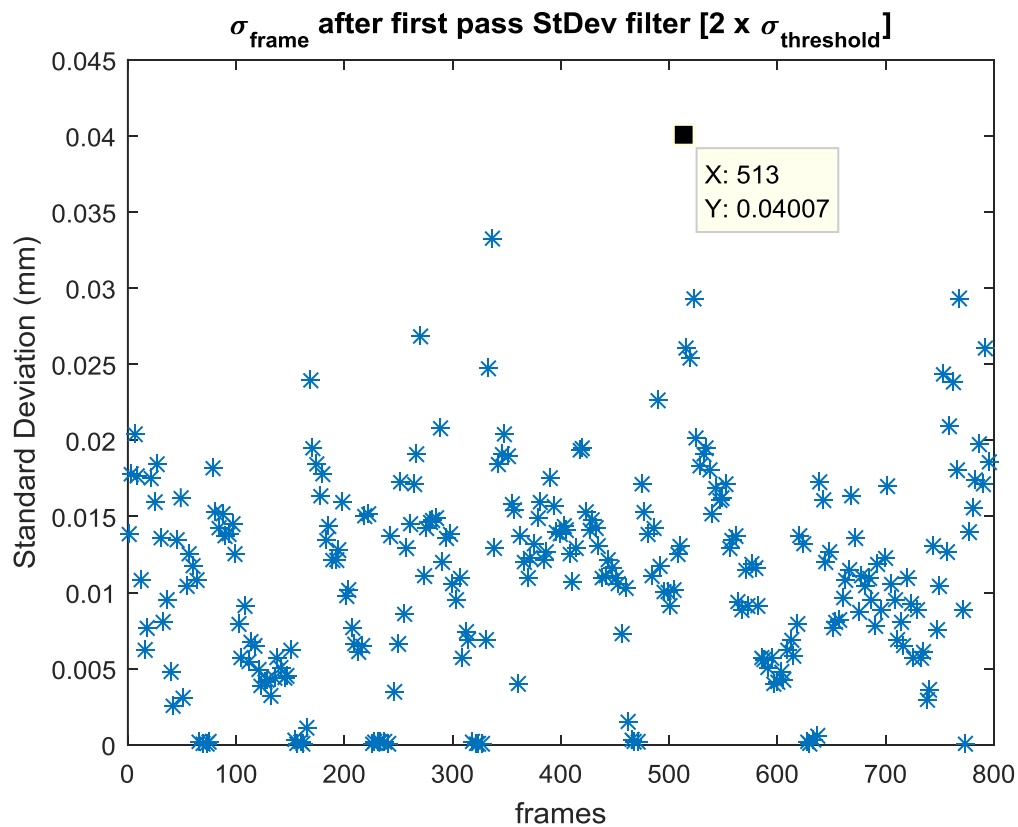


Figure 3.10) Standard Deviation for each frame over entire collect – 1st pass StDev

Frame 774 and other frames that failed to meet the threshold have been set to zero. The offending frames will be pegged at 0 for now to allow further post-processing.

The problem with this method is a single outlier can drastically skew the $\sigma_{threshold}$ value such that only that single outlying frame could be filtered out. After observation it was clear that more frames would need to be filtered out. Frame 513 is the frame with the highest standard deviation value remaining in the set. This frame is shown in Figure 3.11.

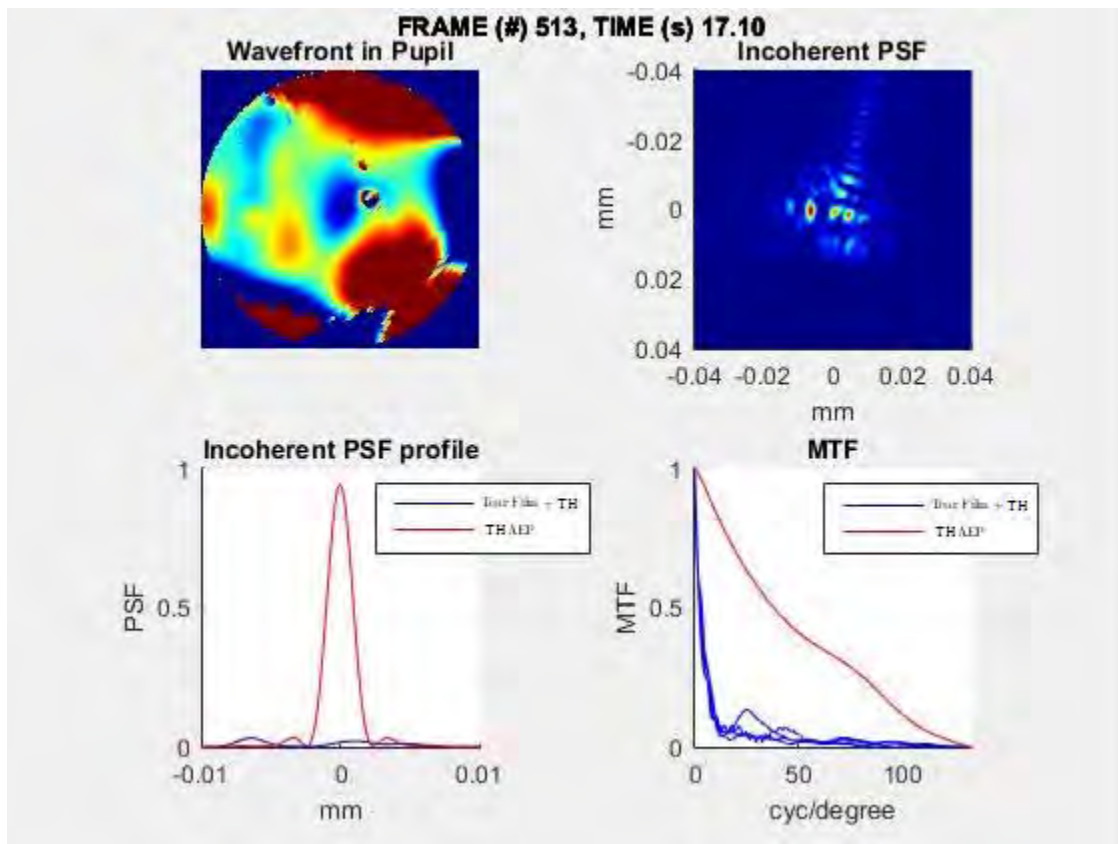


Figure 3.11) Movie snapshot for frame 513 highlighted in Figure 3.11

Frame 513 contains more useful data than frame 774, but it is sufficiently noisy such that further filtering is needed for this frame and other frames like it. The solution chosen was to perform the standard deviation filter once again. This filter can now be referred to as the double pass filter. The same operation is performed on the remaining set of data. Figure 3.12 shows the set after a second

pass, and this operation happens automatically when the StDev threshold value is set to a non-zero input.

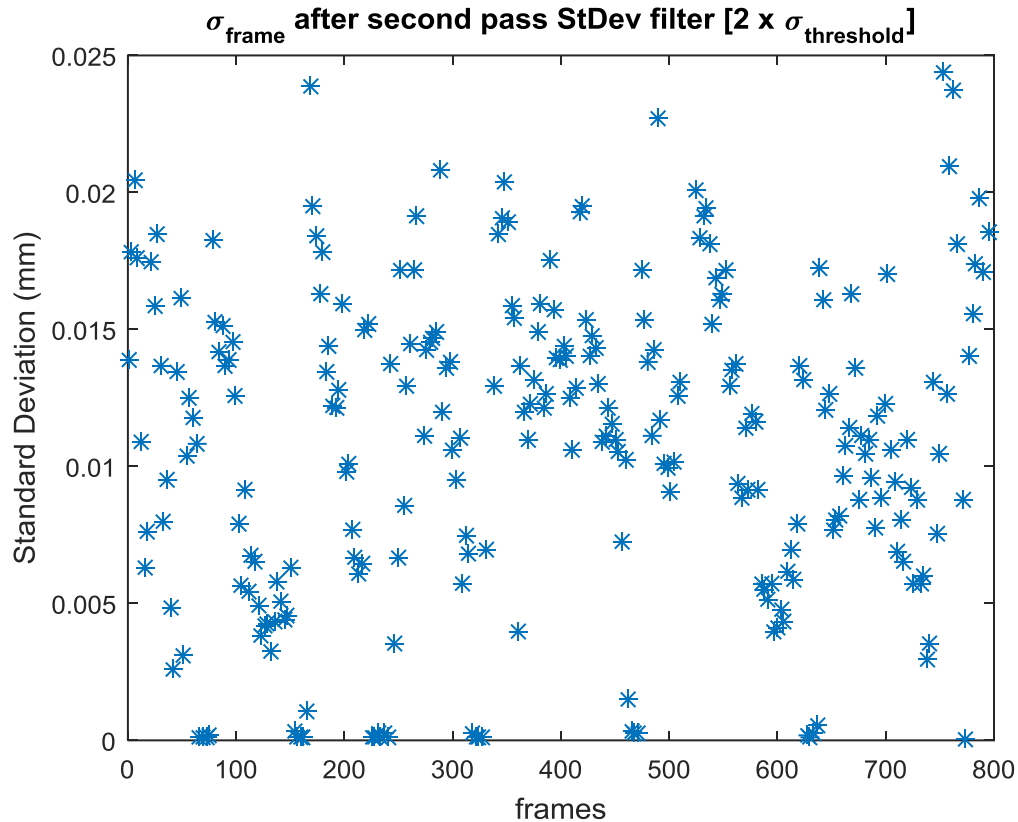


Figure 3.12) Standard Deviation for each frame over entire collect – 2nd pass StDev

Frame 513, along with a few others, have been filtered out. This filtering method does a good job at filtering out the noisiest frames, but still some bad frames remain. For a quicker and more stringent option, an auto standard deviation filter was created.

The auto standard deviation filter is much simpler. The checkbox shown in Figure 3.4 is a hard coded filter that eliminates any frame that has a σ_{frame} below .002 mm or above .02 mm. It is performed after the double pass operation described above. These values were determined from empirical observation and seemed to work well for most data sets. In the case that they don't, the double

pass standard deviation input is still available. Figure 3.13 shows the set after the auto standard deviation filter.

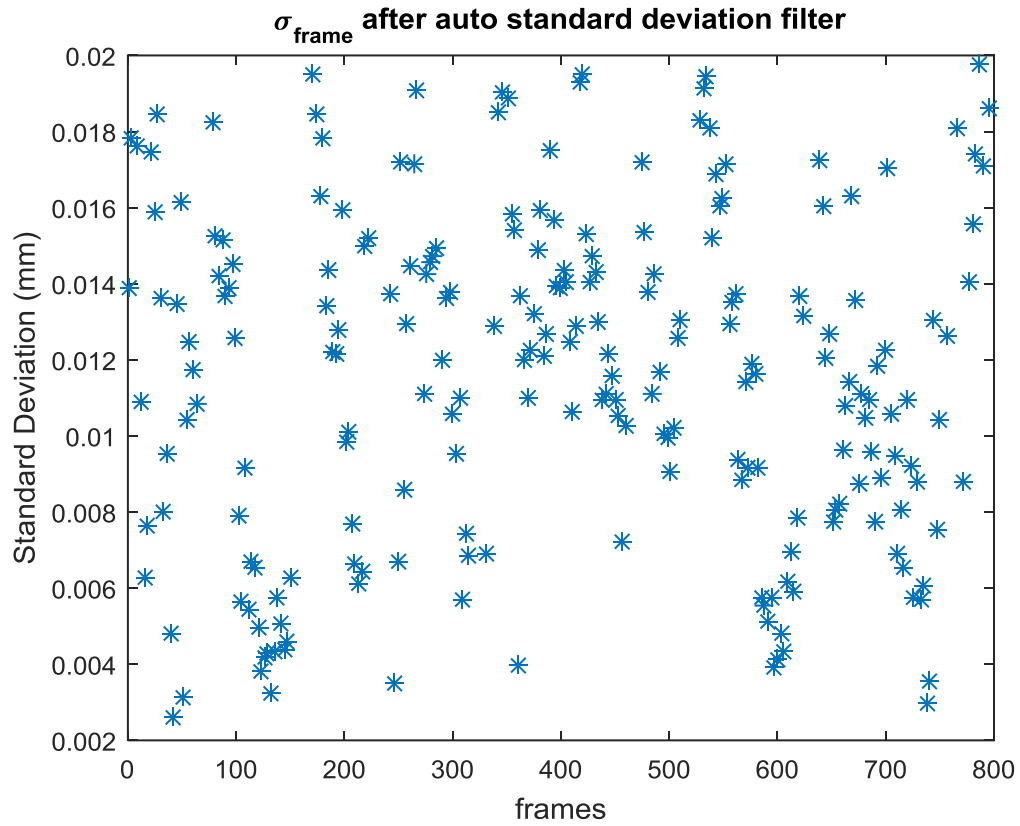


Figure 3.13) Standard Deviation for each frame over entire collect – auto standard deviation filter

3.2.3 COMBO FILTER

The following arrangement of charts displays clearly the effectiveness of the filtering system. Shown is the raw data SQF (top), the SQF with each filter applied separately (left and right), and finally with both SQF and StDev filters applied (bottom). This is referred to as the combo filter.

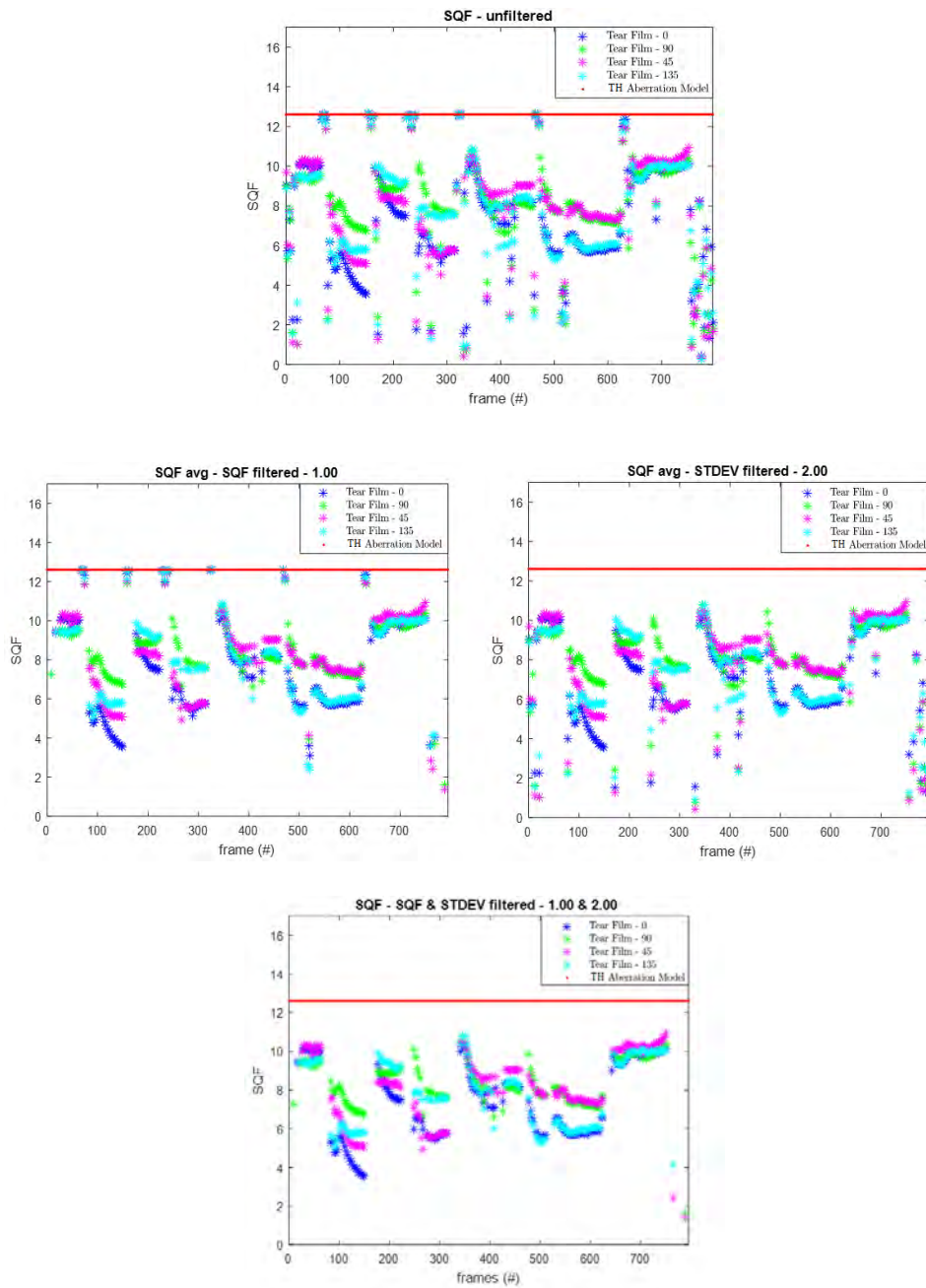


Figure 3.14) SQF charts: Unfiltered (top), SQF filtered (left), standard deviation filtered (right), and combo filter (bottom)

Figure 3.14 shows that the two filters find different types of bad frames to eliminate. When the inputs are chosen wisely, the remaining data set is much cleaner and tear film behavior can be determined more easily.

3.2.4 OTHER OPTIONS

The options remaining can be classified as display options. Two different options are available for the dependent axis variable: time or frames. The SQF data can be displayed as the four different meridional cuts or as an average of all four. The four meridionals can sometimes indicate certain features appearing in the tear film, whereas the average is a less visually busy and sometimes better for an overall general assessment.

3.2.5 END CONDITIONS

When the operation is complete, the user will be shown both the unfiltered and filtered versions of the SQF. This will allow the user to determine if proper filtering conditions were applied (Figure 3.17). The user will also be prompted with a message (Figure 3.15) to reset the filtering conditions and rerun the process, or to complete the data run and save the SQF charts and a new filtered movie. Figure 3.16 shows a diagram of the process to make it clearer.

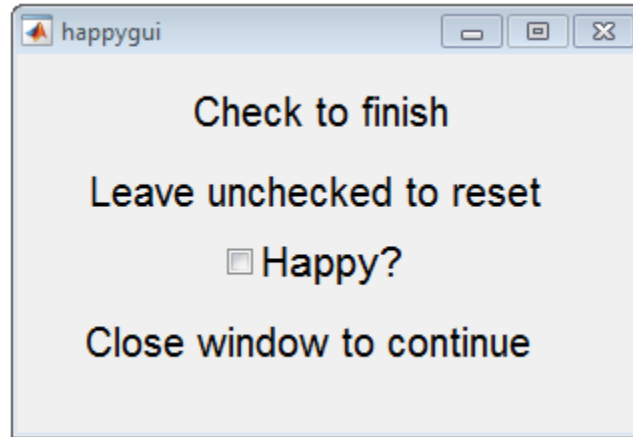


Figure 3.15) Post processing end condition GUI

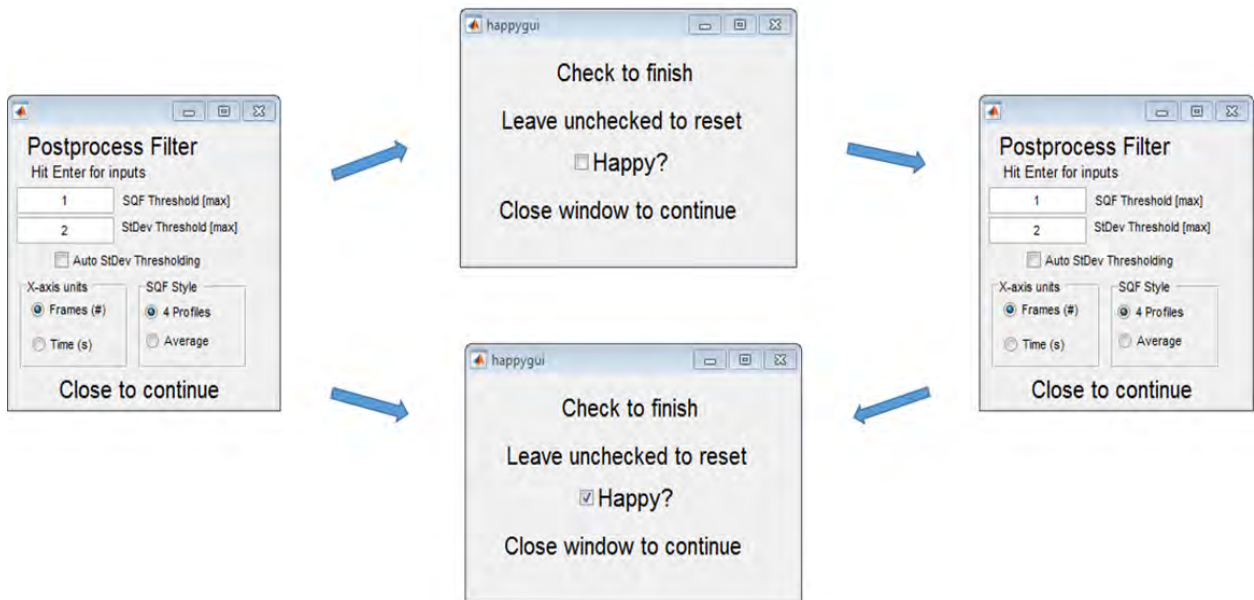


Figure 3.16) Post Processing script cycle

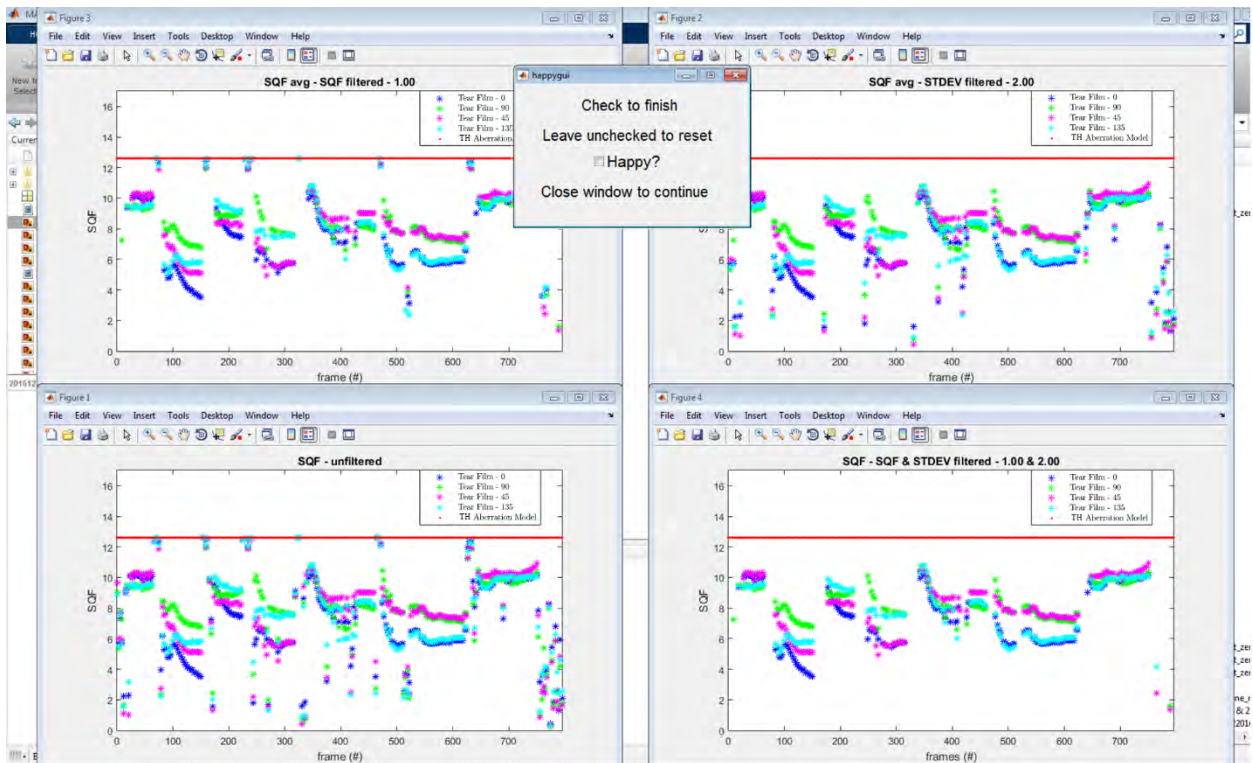


Figure 3.17) Subject 002 – 201508 – Collect 4: This step in the analysis helps the user determine if the filter conditions set previously were acceptable.

Figure 3.17 shows how the program will display the different filtering charts when it is run in MATLAB. These charts are the same ones shown in Figure 3.14. Comparing the bottom left and bottom right corners, the data set has been significantly cleaned up.

These two scripts in tandem make it possible for any data set to produce a movie displaying the 2D Incoherent PSF, PSF line profile, and 4 MTF line profiles over the entirety of a collect, as well as an SQF chart. The code has the capability to produce downsampled collects in the interest of data compression. As stated earlier in this report, the TFI takes data at 30 FPS, and movies have been produced that show data at 10 FPS.

4.0 RESULTS

4.1 MOVIES AND SQF CHARTS

As discussed previously, this PSF is the result of the tear film surface minus a biconic fit, but plus the TH aberration eye model. The incoherent PSF and MTF line profiles that follow are the result of taking a single horizontal line profile across the center of the Incoherent PSF. The SQF charts are the area under those line profile curves, integrated over a 3 to 18 cyc/degree range of spatial frequencies.

The following figures show the SQF charts after they've been filtered through the post-process software described in Section 3.0.

As stated earlier, the data sets shown below are processed with sixteen Zernike fit removals and no reverse ray tracing. The pupil size chosen for this analysis was 4.5 mm.

The orange circles were manually inserted to indicate blink occurrences. Blinks were determined by watching the visual quality movie associated with the collect. Contextual clues such as a brief loss of data followed by a significant change in tear film behavior clearly indicate where blinks occurred during the collect.

4.1.1 SUBJECT 002

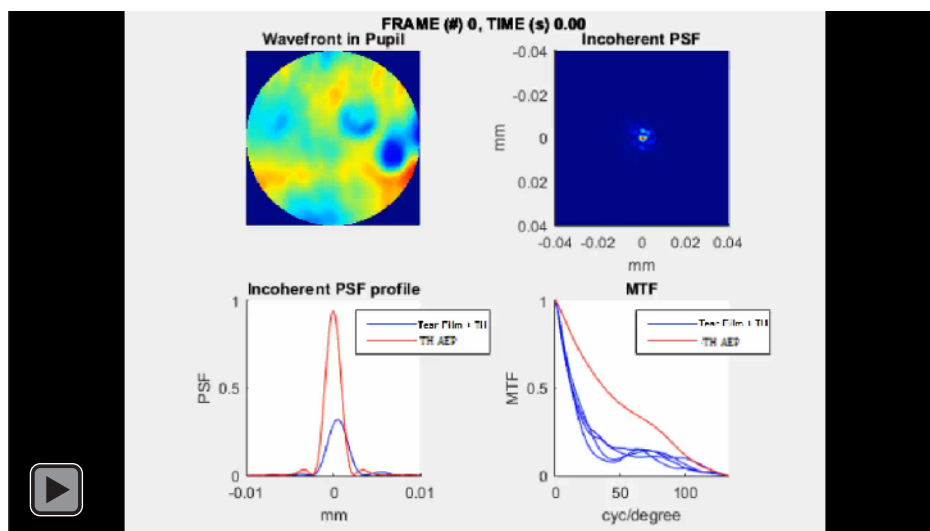
Figure 4.1 is added confirmation to the hypothesis that started this project. The tear film SQF is significantly affected compared to the TH aberration model SQF (redline in Figure 4.1).

The visual quality of Subject 002 decreases after the first blink before frame 100. The visual quality continues to degrade until the subject's second blink. The second blink provides a significant improvement in visual quality, but post blink starts to degrade once more. The 3rd, 4th, and 5th blinks provide even quicker spikes in visual quality followed by even steeper drop-offs.

The sixth and final blink in this collect improves the visual quality back to the baseline SQF seen at the beginning of the collect.

This blink -> rise -> fall -> stabilize -> blink loop has some interesting implications. The blinks seem so intricately linked to visual quality behavior, it becomes reasonable to assume that visual quality is being used to regulate blink rate.

This data set also shows that not all blinks are created equal. Since the subject was often instructed to attempt to keep their eyes open, it seems likely many of these blinks were partial. The blinks in the middle of the data set show a sharp rise and followed by a sharp fall. The tear film could be only partially resetting due to a partial or weak blink (Benedetto, Clinch & Laibson, 1984). This means that the temporary visual quality increase is fragile, and is likely to degrade quickly. It is likely that the blink at the end of the collect was a fuller blink, that reset the tear film in such a way that the visual quality could return to baseline.



Video 4.1) Subject 002 – 201508 – Collect 4 Movie

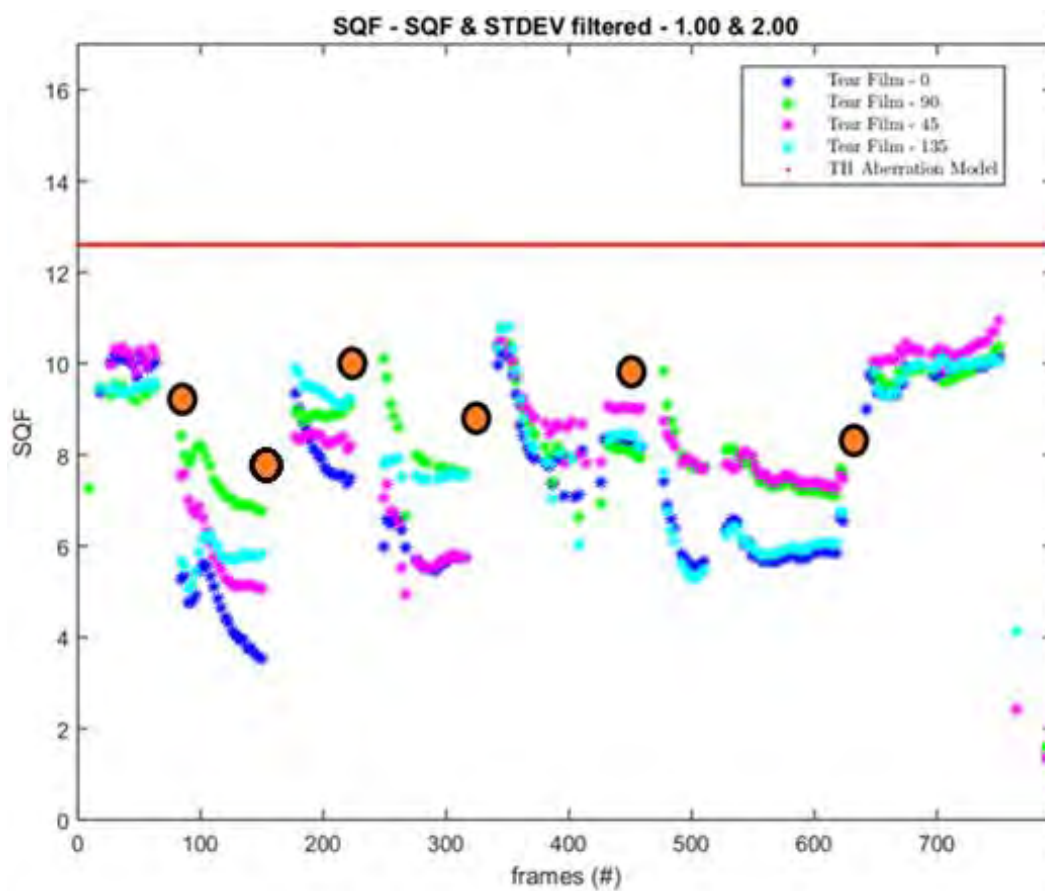
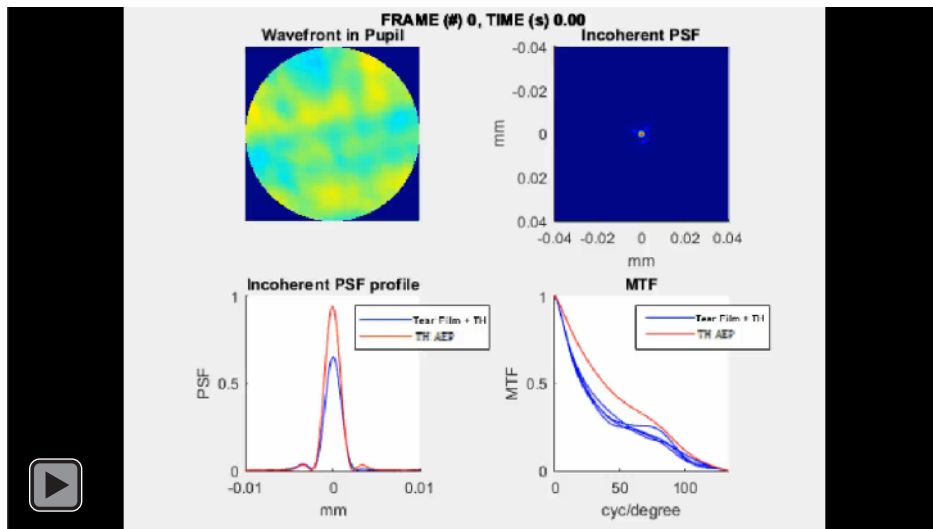


Figure 4.1) Subject 002 – 201508 – Collect 4 SQF Chart

Total collection time: 27 seconds

Figure 4.2 is a data set from the same subject as Figure 4.1 taken on the same day. This collect shows some different behavior. Although the tear film still follows the general blink \rightarrow rise \rightarrow fall trend, the tear film in this collect is a little bit more predictable and continuous. The average SQF for this collect is significantly higher than for Figure 4.1. This tear film can be said to be more stable than the tear film in the previous one. These two data sets together show how much a person's tear film can vary even over the course of a couple minutes.



Video 4.2) Subject 002 – 201508 – Collect 8 Movie

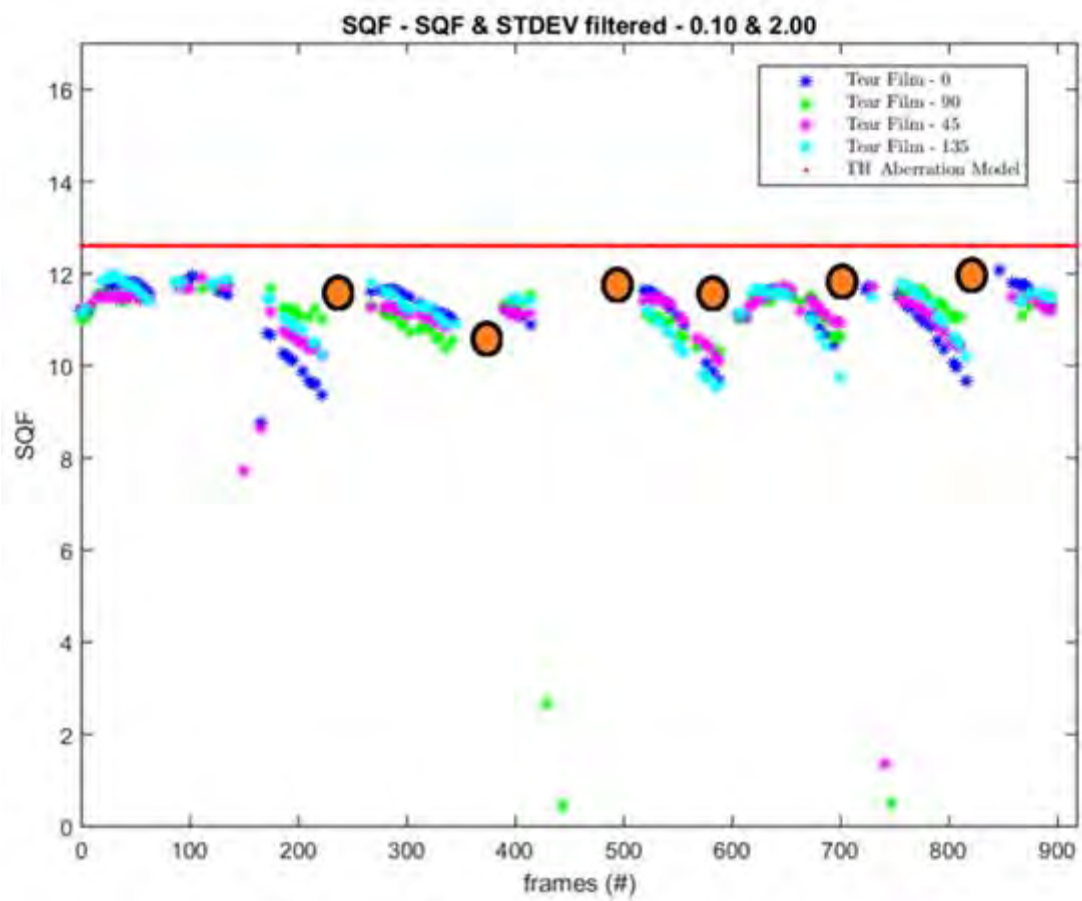


Figure 4.2) Subject 002 – 201508 – Collect 8 SQF Chart

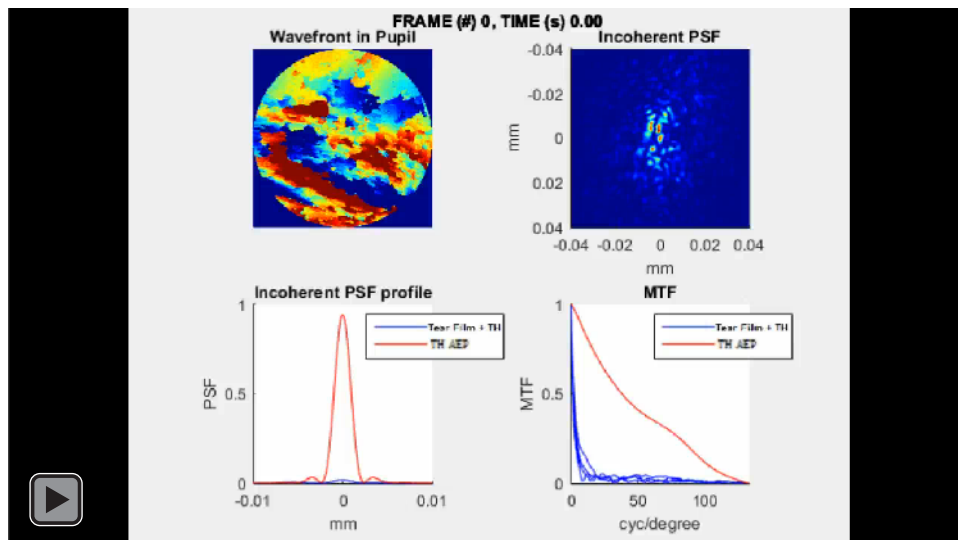
Total collection time: 31 seconds

4.1.2 SUBJECT 007

Figure 4.3 shows an example of an extremely stable tear film. Subject 007 managed to maintain data integrity throughout the entirety of the collect. There was a very gradual decrease in visual quality behavior before a blink was needed. While Subject 002 took a blank every 100 frames, Subject 007 took a blank every 1,000 frames.

This data set again provides more weight to the idea that visual quality and blink rate are connected. Subject 002 experienced a significantly degraded visual quality, and had to fight off blinks for most of the collect. Subject 007 had almost no visual degradation from tear film surface, and hence had no trouble keeping an eye wide open.

It also is interesting to see how much the tear film behavior varies from person to person. It was observed with Subject 002 that tear film behavior could vary significantly from collect to collect, but this shows that it also varies significantly from subject to subject.



Video 4.3) Subject 007 – Collect 1 Movie

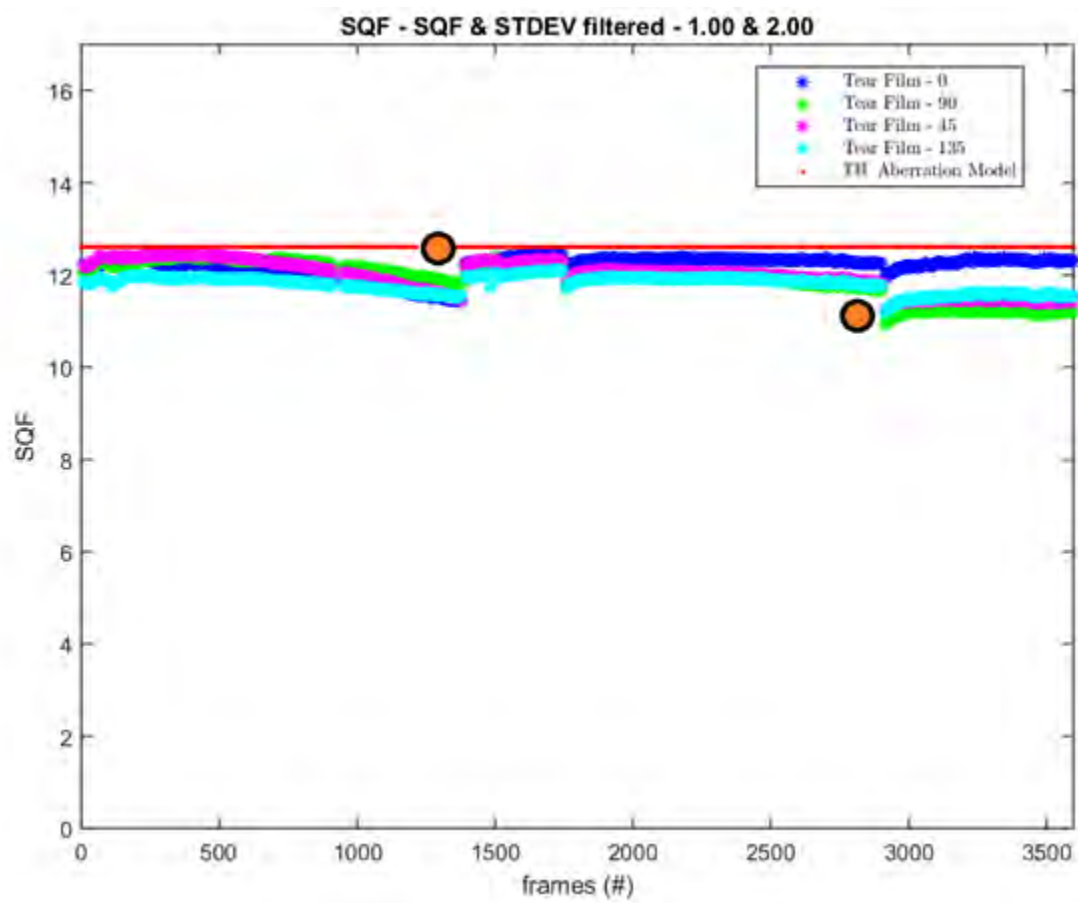


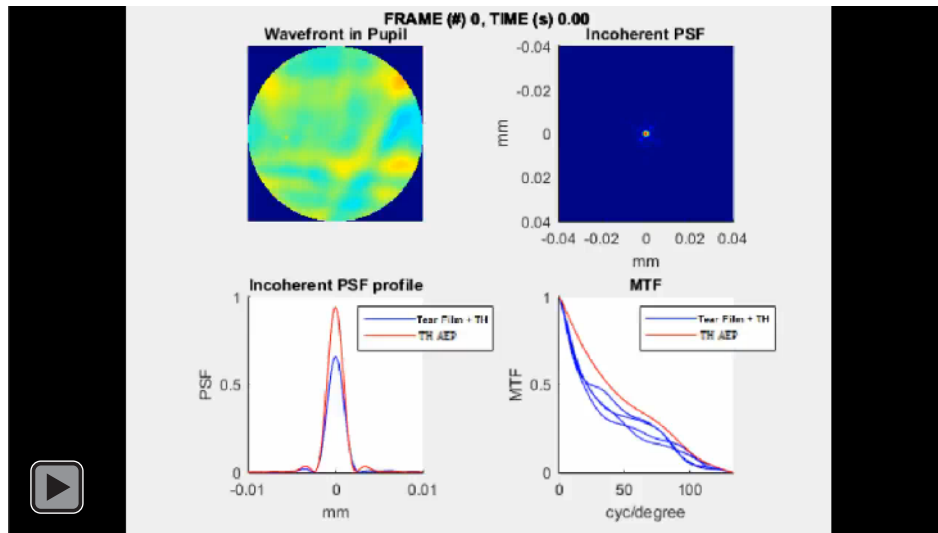
Figure 4.3) Subject 007 – Collect 1 SQF Chart

Total collection time: 120 seconds

4.1.3 SUBJECT 009

Figures 4.4 and 4.5 show that Subject 009 has similar tear film behavior to Subject 007. The tear film is resilient, maintains data integrity throughout most of the collect, and delivers a high SQF value.

These very stable tear films may not be entirely rare.



Video 4.4) Subject 009 – 201507 – Collect 3

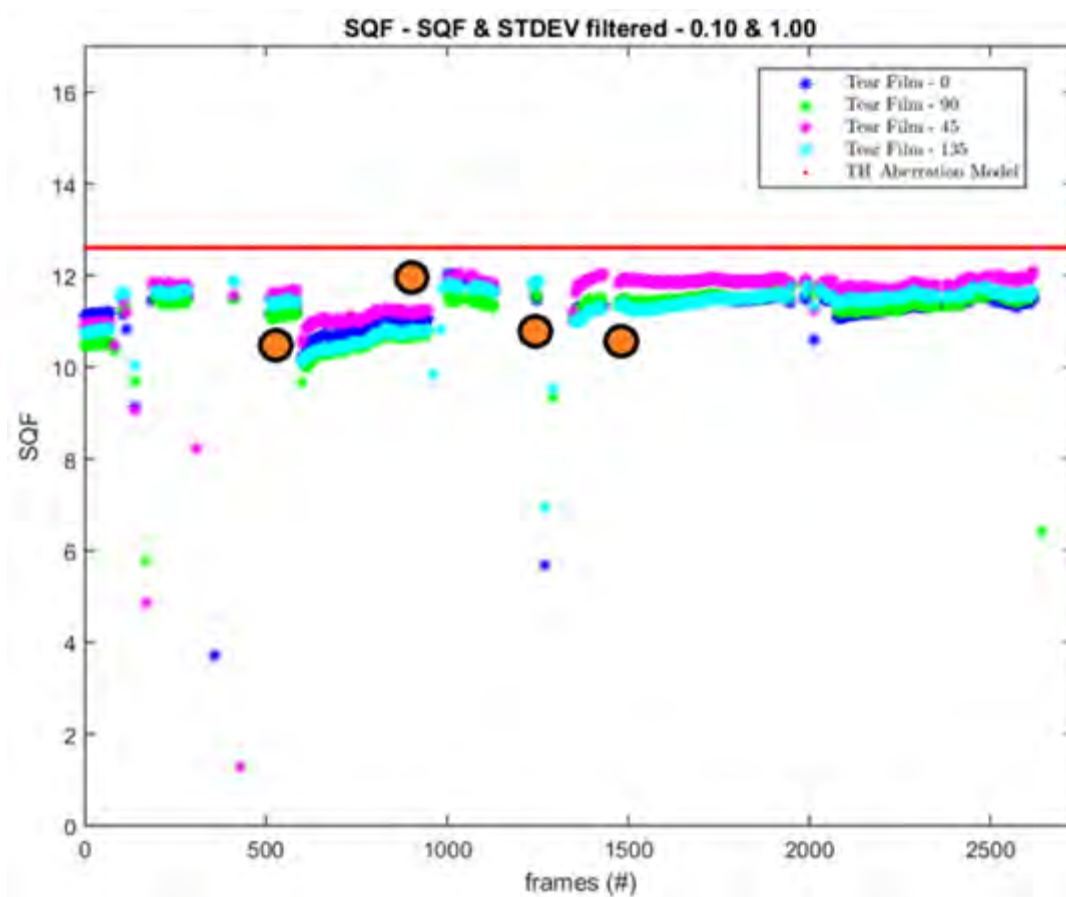
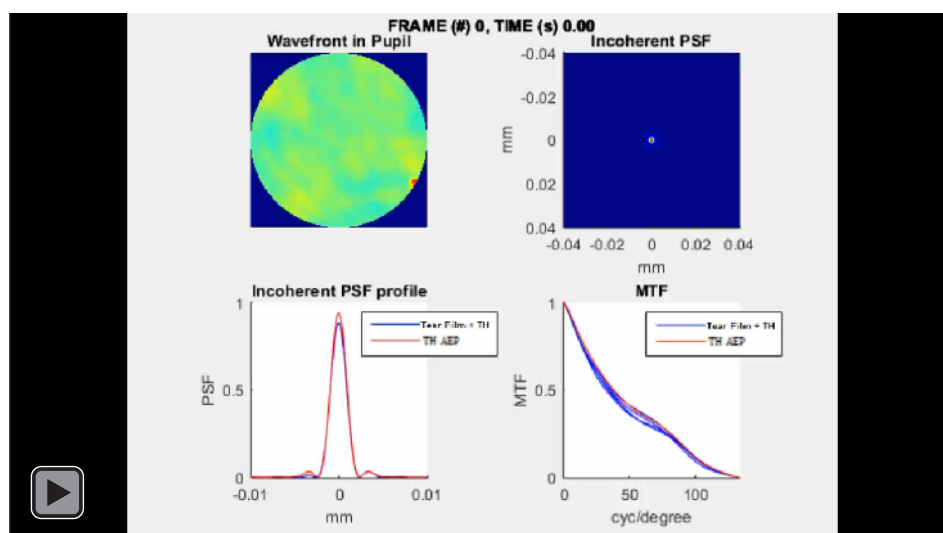


Figure 4.4) Subject 009 – 201507 – Collect 3 SQF Chart

Total collection time: 91 seconds



Video 4.5) Subject 009 – 201507 – Collect 8 Movie

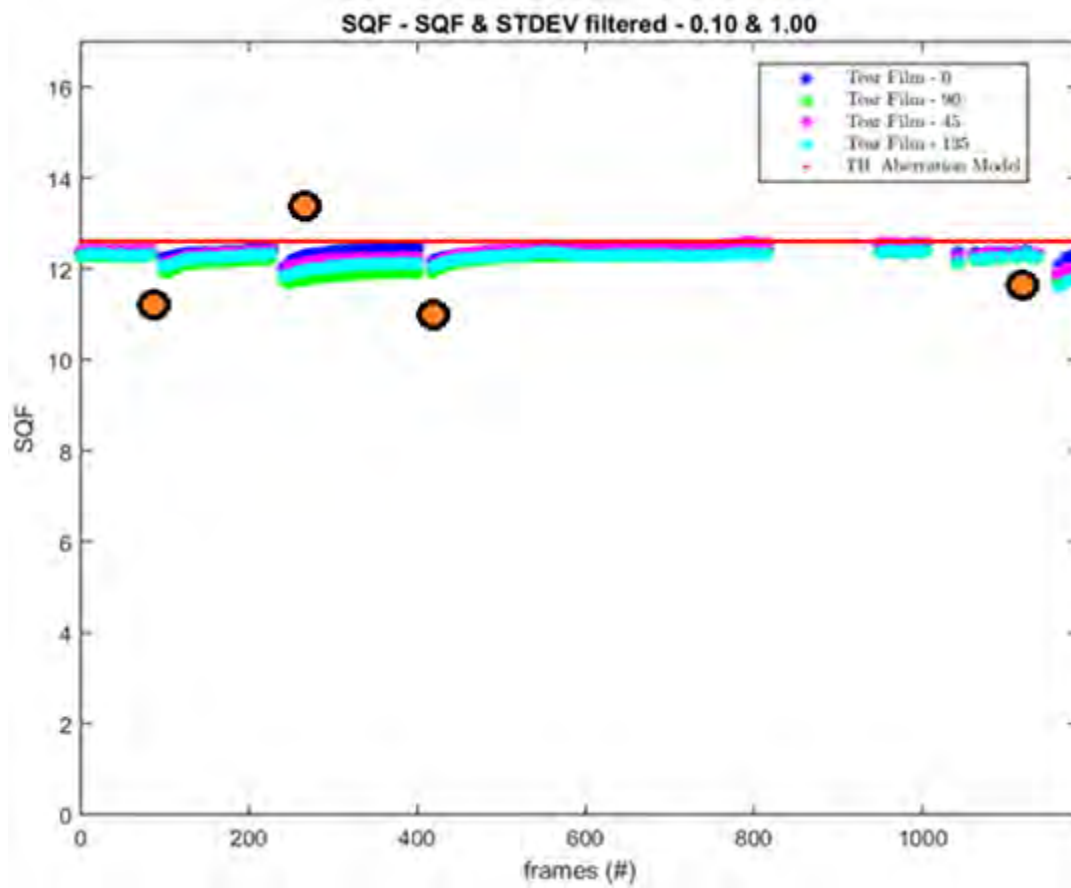
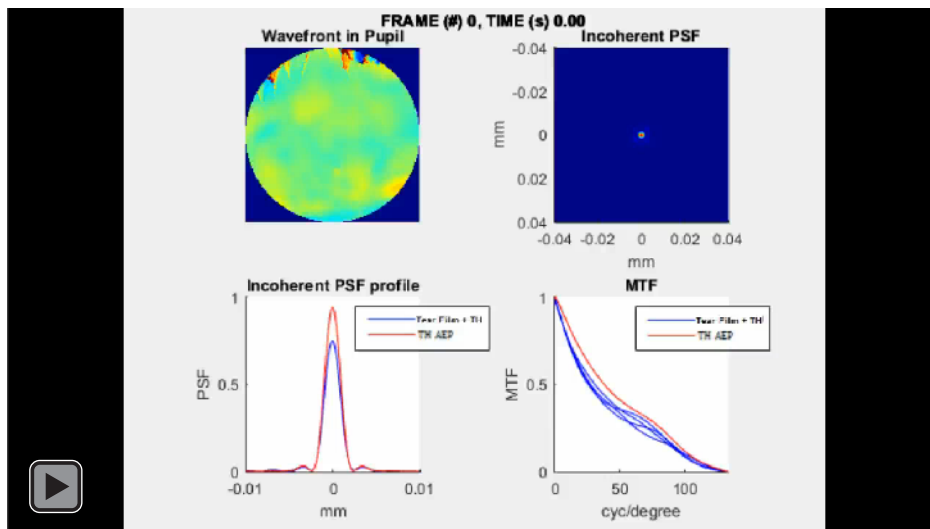


Figure 4.5) Subject 009 – 201507 – Collect 8 SQF Chart

Total collection time: 40 seconds

4.1.4 SUBJECT 010

Figure 4.6 is a good example of another useful feature of this type of analysis. Of all subjects tested, Subject 010 exhibited the most drastic SQF displacement across the different angled cuts. Starting around frame 1100 a blink occurs, and the four SQF metrics separate significantly. This separation is caused by the appearance of a blink line feature in the tear film. This feature can be seen in Figure 4.6 which is a snapshot from the data set. The snapshot on the top shows the tear film behavior before the 1100 blink, and the snapshot on the bottom show it after.



Video 4.6) Subject 010 – 20150513 – Collect 12 Movie

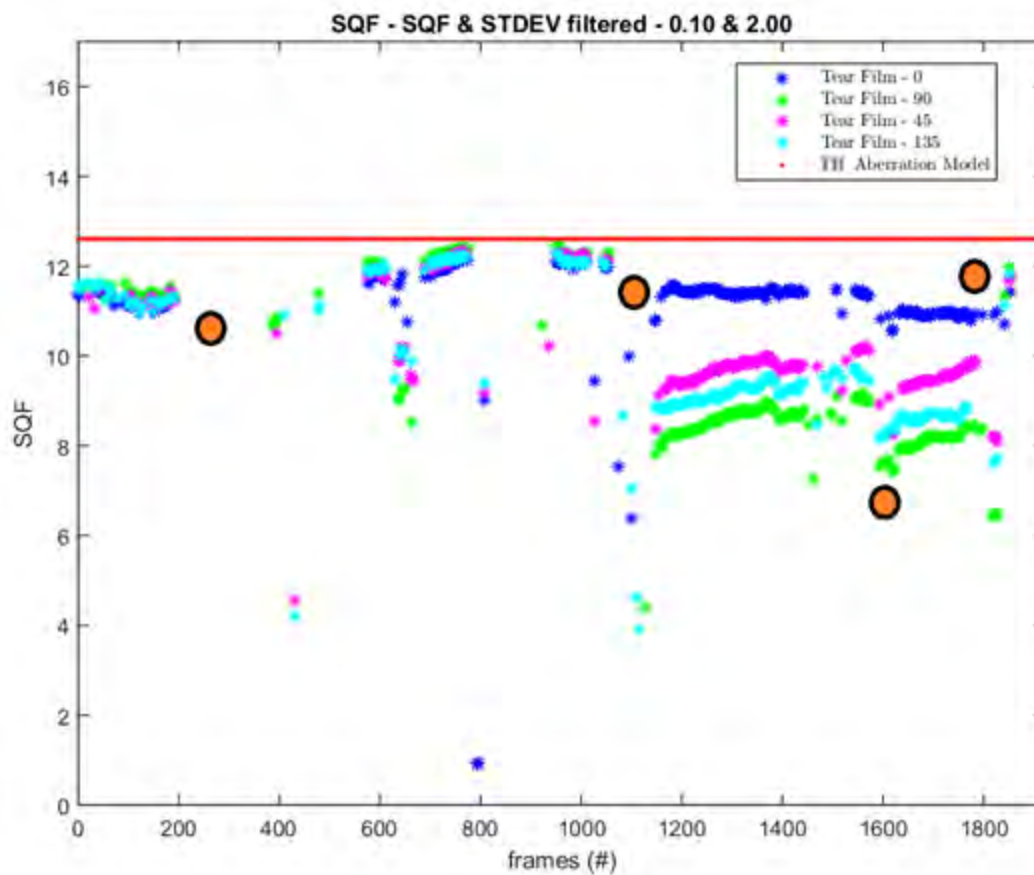


Figure 4.6) Subject 010 – 20150513 – Collect 12 SQF Chart

Total collection time: 64 seconds

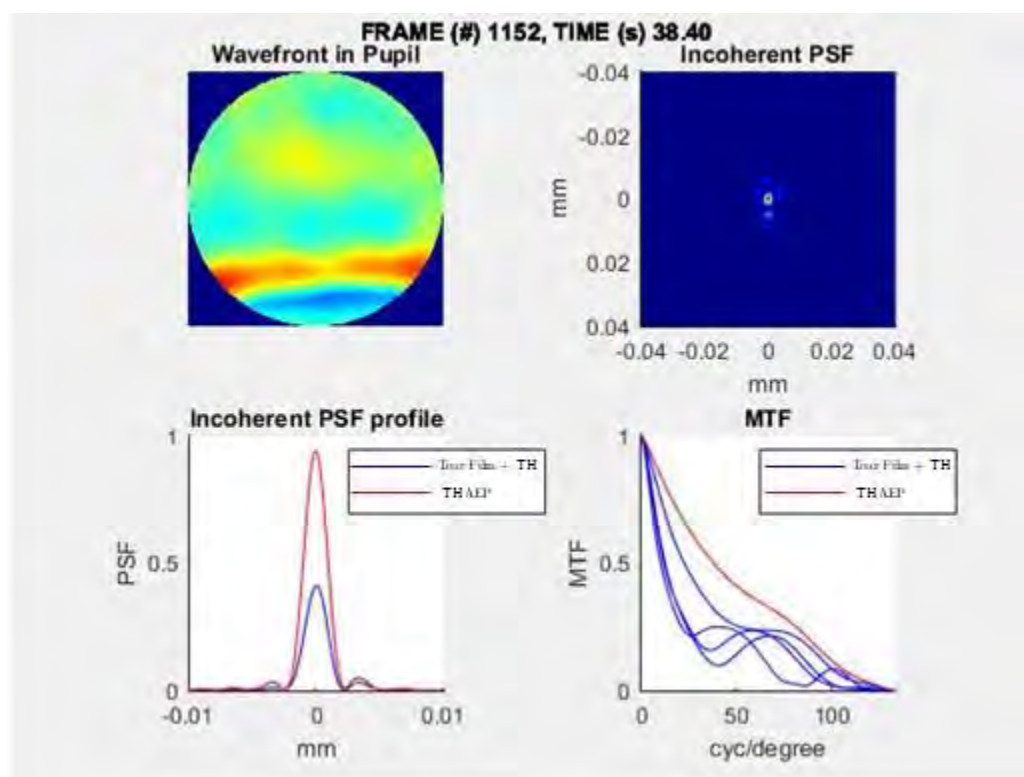
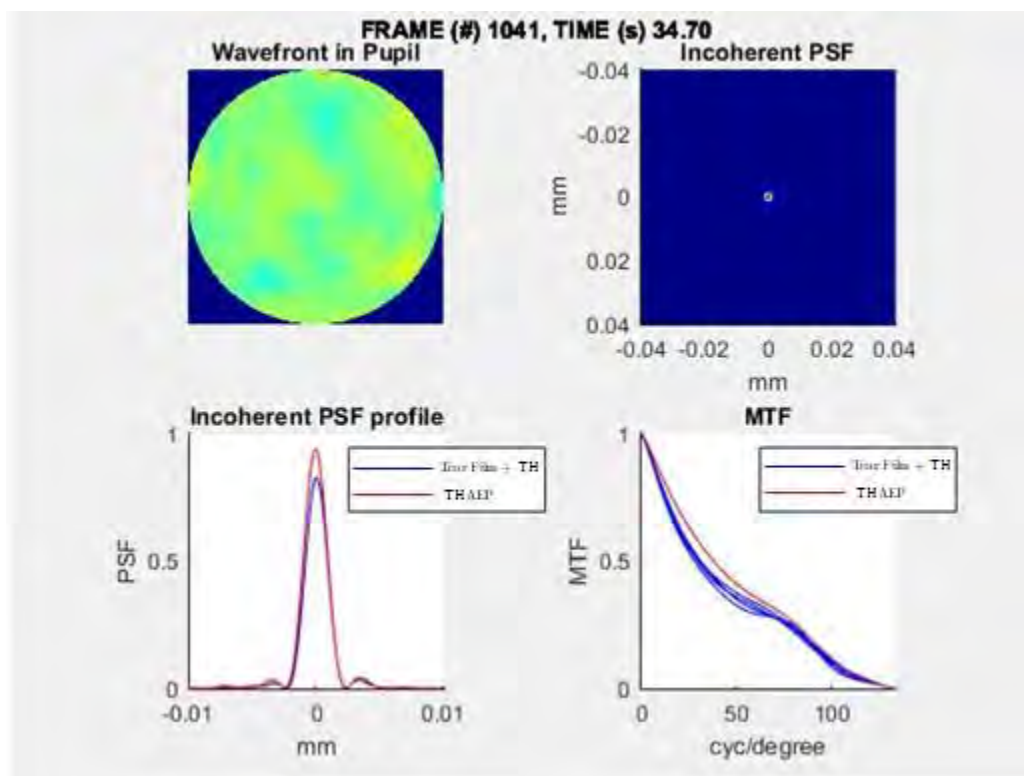


Figure 4.7) Movie Snapshots for frames 1041 (top) and 1152 (bottom) for Subject 010 – Collect 12 - shown in Figure 4.6

After looking at the blink line in Figure 4.7 (bottom) the strange SQF separation in Figure 4.5 is now better understood. The blink line is a horizontal feature. This means it will most drastically affect the vertical spatial frequencies. The horizontal line profile, displayed in blue in Figure 4.6, is almost unaffected. The cut that sees the most drastic degradation is the 90-degree vertical profile. The two angled profiles see about the same amount of degradation. The results agree with the intuition.

These results indicate that SQF behavior could be used to predict tear film features.

5.0 POTENTIAL IMPROVEMENTS

Taking the valuable qualitative observations and turning them into more concrete, quantitative ones would be useful. A good place to start this process would be automating blink detection from the SQF charts, such that the big orange circles would be automatically placed as opposed to the manual placement that was used to create them for this report. That would save the time it takes to cross reference the SQF chart with the visual quality movie to determine where the blinks are.

Once the blink times are stored, the behavior of the SQF function between blinks can be more easily quantified. A simple regression analysis could be performed on the set of points between blinks to determine the coefficients for a function that fits the behavior. Storing all these fitted functions would allow a quantified analysis of tear film behavior after blinks across different subjects.

Clinical correlations could be studied. Dry eye is a condition that involves both the lack of secretion from glands in the eye, but also the rapid evaporation of the tear film (Baudouin, C. & Aragona, P. & Messmer, E.M. *et al.* 2013). The dry eye disease cycle is a difficult problem to get a handle on due to

the many factors that influence the tear film behavior. The scope of this problem is shown by Figure 5.1.

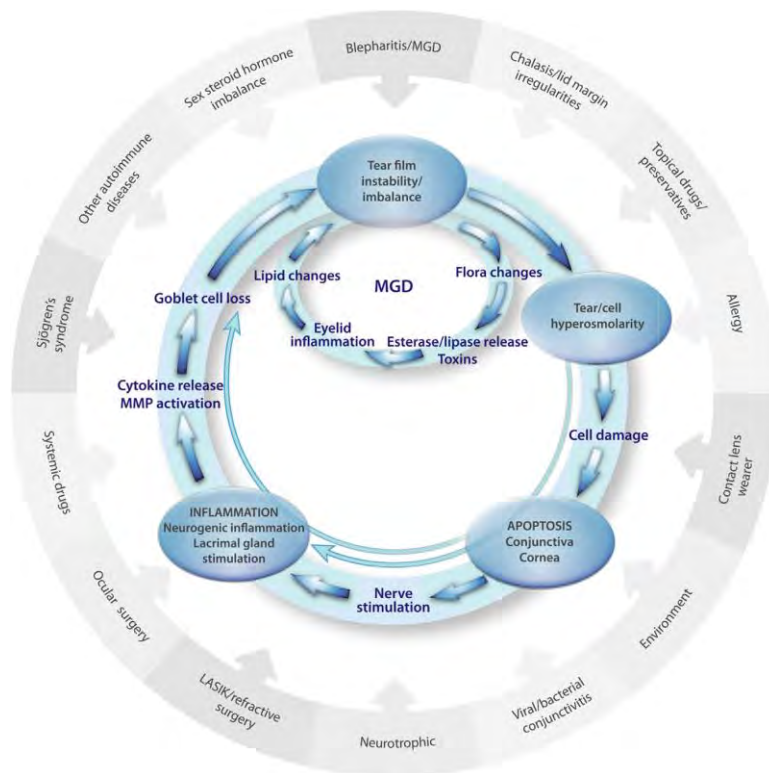


Figure 5.1) Dry Eye Disease Cycle
(Baudouin, C. & Aragona, P. & Messmer, E.M. et al. 2013)

Due to the dynamic quality of the TFI measurements, the analysis method used in this report could be especially useful to better understand the tear film behavior of those who suffer from chronic dry eye. The problem is so large in extent with so many variables that quantification is necessary to make progress. This analysis method should assist in that effort.

6.0 CONCLUSIONS

Software was written that successfully turns tear film topography into visual quality metrics. Visual quality movies were created showing how the incoherent PSF, MTF, and tear film change over time. SQF charts for the course of the collect were created that yield many interesting qualitative observations of tear film behavior. 30 FPS collects were turned into 10 FPS movies, reducing the amount of data needed to make meaningful conclusions.

As stated in the introduction, this is not the first time that it has been proven that tear film topography, specifically tear film break up, significantly degrades the PSF of the human eye (Kasprzak & Licznerski, 1999). This project strongly supports that conclusion, while also taking steps forward. Rather than a simulation, this conclusion was proven with measured tear film data. Several subjects and long data runs allowed for a larger sample size, which increases the amount of evidence to support this conclusion by several orders of magnitude.

The SQF charts help show the relationship between blinks, visual quality, and the tear film. The blink dependent visual quality cycle shown in Figures 4.1 and 4.2 for Subject 002 appears to share a relationship with tear film thickness. A previous study measured the thickness of the tear film as a subject blinked (Benedetto, Clinch & Laibson, 1984). The result of that is shown in Figure 6.1. The arrows indicate the decreasing thickness between blinks.

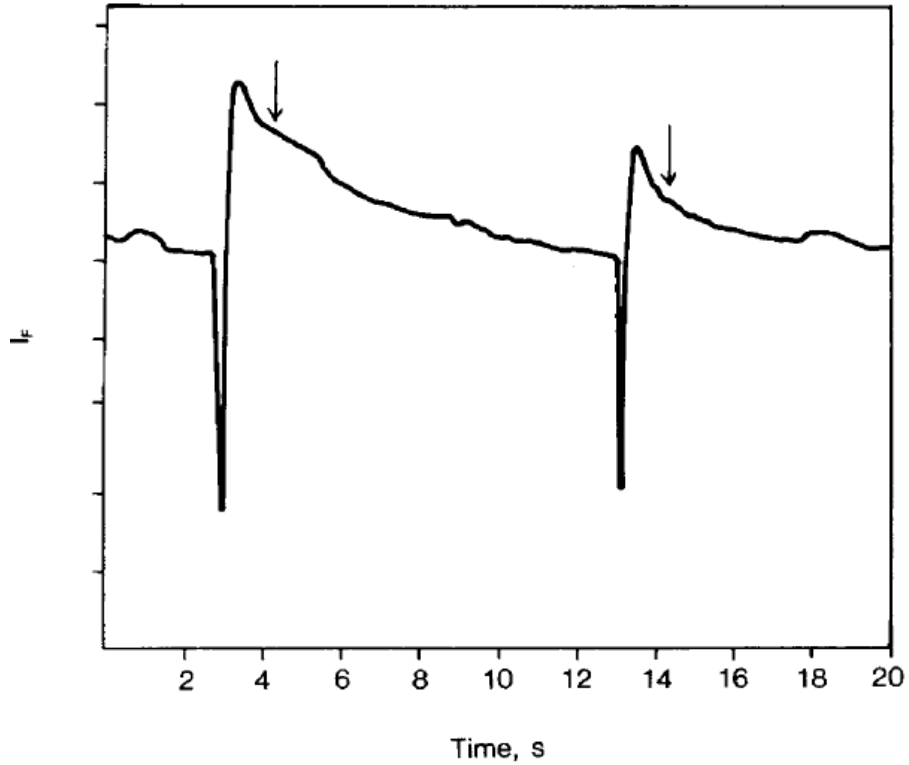


Figure 6.1) Intensity of fluorescence or tear film thickness over time
(Benedetto, Clinch & Laibson, 1984)

Although this thickness degradation behavior was present in a few subjects, most of the patients exhibited much more consistent tear film behavior over the course of the collect. This is shown in Figure 6.2, and could correlate with patients like subjects 007 (Figure 4.3) and 009 (Figures 4.4 and 4.5).

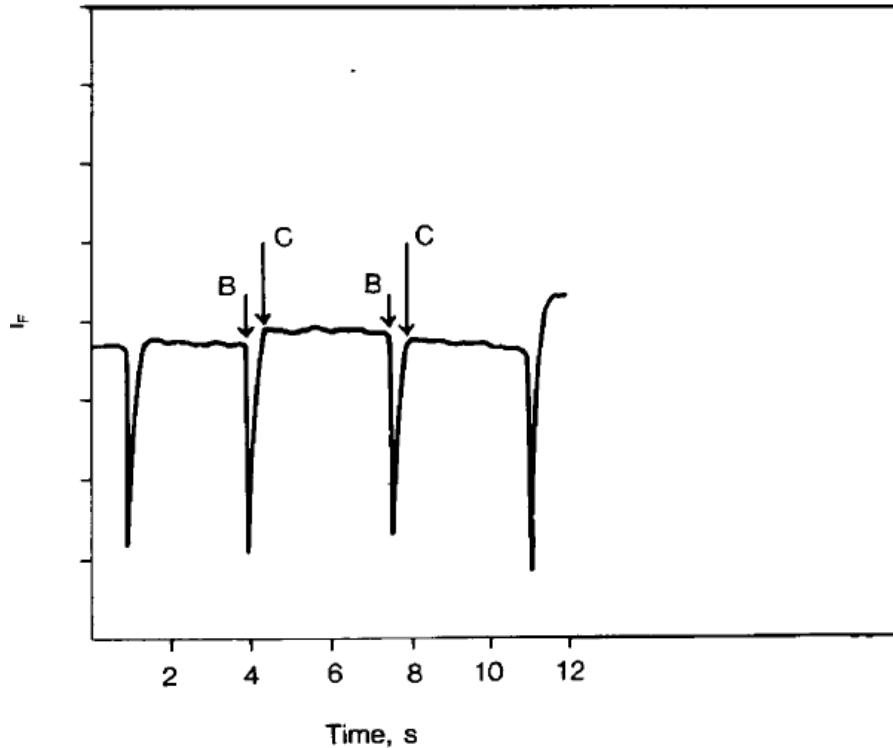


Figure 6.2) Intensity of fluorescence or tear film thickness over time. B: lid closure; C: lid opening; B-C interval: blink. (Benedetto, Clinch & Laibson, 1984)

The software written for this thesis provides a tool that further explores this blink/vision/tear film relationship, and this has several potential applications. Blinking plays an important role in the stabilization of the tear film (Benedetto, Clinch & Laibson, 1984), and characterization of breakup behavior could be used to diagnose and treat dry eye to help with the physical discomfort associated with an abnormal tear film (Holly, 1980). The contact lens has a significant impact on the behavior of the tear film (Muntz, Subbaraman, Sorbara & Jones, 2015). Analysis of visual quality could be used to determine the effectiveness of a contact lens shape or material to coexist with the tear film. These are two important areas of further research that this tool creates potential for.

7.0 REFERENCES

- Barten, P. G. J. (1990). Evaluation of subjective image quality with the square-root integral method. *Journal of the Optical Society of America A*, 7(10), 2024–2031.
Retrieved from <https://www.osapublishing.org/josaa/abstract.cfm?&uri=josaa-7-10-2024>
- Baudouin, C. & Aragona, P. & Messmer, E.M. *et al.* (2013). Role of hyperosmolarity in the pathogenesis and management of dry eye disease: proceedings of the OCEAN group meeting. *The Ocular Surface*, 11(4), 246–258. doi: 10.1016/j.jtos.2013.07.003
- Benedetto, D., Clinch, T. E., & Laibson, P. R. (1984). In vivo observation of tear dynamics using fluorophotometry. *Archives of Ophthalmology*, 102(3), 410–412.
doi: 10.1001/archoph.1984.01040030328030
- Daily, L., & Coe, R. E. (1962). Lack of effect of anesthetic and mydriatic solutions on the curvature of the cornea. *American Journal of Ophthalmology*, 53, 49–51.
Retrieved from <http://www.sciencedirect.com/science/article/pii/0002939462903951>
- Granger, E.M. & Cupery, K.N. (1972). An optical merit function (SQF), which correlates with subjective image judgments. *Photographic Science and Engineering*, 16, 221-230.
- Holly, F. J. (1980). Tear film physiology. *American Journal of Optometry and Physiological Optics*, 57(4), 252–257.
- Kasprzak, H. T., & Licznarski, T. (1999). Influence of the characteristics of tear film break-up on the point spread function of an eye model. *Proceedings of SPIE*, 3820, 390–396.
Retrieved from <http://proceedings.spiedigitallibrary.org/proceeding.aspx?articleid=906549>
- Kiely, P. M., Smith, G., & Carney, L. G. (1982). The mean shape of the human cornea. *Journal of Modern Optics*, 29(8), 1027–1040. doi: 10.1080/713820960
- Micali, J. D. (2015). *Interferometer for Measuring Dynamic Corneal Topography*.
- Muntz, A., Subbaraman, L.N., Sorbara, L., Jones, L. (2015). Tear exchange and contact lenses: a review. *Journal of Optometry*, 8, 2–11. doi: 10.1016/j.optom.2014.12.001
- Primeau, B. C. (2011). *Interferometric Characterization of Tear Film Dynamics*.
- Porter, J. & Guirao, A. & Cox, I.G. & Williams, D. (2001). Monochromatic aberrations of the human eye in a large population. *Journal of the Optical Society of America A*, 18(8), 1793-1803.
doi: 10.1364/JOSAA.18.001793
- Schwiegerling, J. T. (2004). *Field Guide to Visual and Ophthalmic Optics*. SPIE Press.
Retrieved from <http://ebooks.spiedigitallibrary.org/content.aspx?bookid=150§ionid=31562194>
- Voelz, D. G. (2011). *Computational Fourier Optics: A MATLAB Tutorial*. SPIE Press.